Petroleum Science 23 (2026) 712–729

Contents lists available at ScienceDirect

Petroleum Science

journal homepage: www.keaipublishing.com/en/journals/petroleum-science

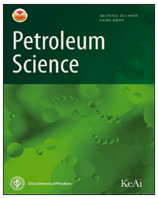

Original Paper

Genesis of Late Carboniferous volcanic rocks in the Kebai Fault Zone, Western Junggar, Xinjiang: Constraints from zircon U-Pb age, whole rock geochemistry, and Sr-Nd-Pb isotopes

Wei Wang [a,b], Chuan-Yi Tang [c], Zong-Quan Yao [a,*], Yan Gao [c], Feng-Bin Han [d], Zong-Rui Xie [c], Jian Chen [a], Yuan-Feng Yang [c], Ya-Fang Zhang [b]

[a] *College of Geological and Mining Engineering, Xinjiang Key Laboratory for Geodynamic Processes and Metallogenic Prognosis of the Central Asian Orogenic Belt, Xinjiang University, Urumqi, 830047, Xinjiang, China*

[b] *Xinjiang Natural Resources and Ecological Environment Research Center, Urumqi, 830000, Xinjiang, China*

[c] *Oil Production Plant of Xinjiang Oilfield Company Baikouquan, Karamay, 834011, Xinjiang, China*

[d] *Institute of Geomechanics, Chinese Academy of Geological Sciences, Beijing, 100081, China*

ARTICLE INFO

Article history:
Received 2 February 2025
Received in revised form
6 July 2025
Accepted 29 October 2025
Available online 4 November 2025

Edited by Min Li

Keywords:
Western Junggar
Kebai Fault Zone
Volcanic rocks
SHRIMP zircon U-Pb chronology
Element/isotope geochemistry

ABSTRACT

The Late Paleozoic tectonic evolution of the Junggar Basin played a critical role in the formation of its oil and gas resources; however, as most of the basin is covered by desert, the evolutionary process remains controversial. In this study, we present a comprehensive analysis of the rock associations, petrography, ages, and systematic elemental and isotopic compositions of Carboniferous volcanic rocks obtained from drilling holes along the western margin of the basin, aiming to better constrain the late Paleozoic tectonic evolution of this region. Two zircon samples, from tuff and andesite layers, yielded concordant ages of 316.8 ± 1.7 and 321.7 ± 1.8 Ma, respectively, indicating intense volcanic eruptions during the Late Carboniferous. The analyzed volcanic rocks exhibited sodic calc-alkaline affinities, with SiO_2 content ranging from 53.46 to 61.57 wt%, TiO_2 content from 0.75 to 1.20 wt%, and a significantly higher Na_2O content than that of K_2O. In terms of trace elements, they showed variable enrichment in light rare earth elements ($(La/Yb)_N = 2.72$ to 7.89) and large ion lithophile elements such as Ba, Th, U, and Sr. Low Cr (0.67–65.72) and Ni (0.86–34.90) contents, together with significant negative Eu anomalies ($\delta Eu = 0.17$ to 0.35), suggest variable fractionation of the primitive magma prior to eruption. All these features, combined with prominent Nb-Ta depletions in PM-normalized incompatible element spider diagrams, unambiguously indicate their genetic relationship with a subduction environment. However, the volcanic rocks showed low initial $(^{87}Sr/^{86}Sr)_i$ values (0.7039–0.7057) and positive $\varepsilon_{Nd}(t)$ values (7.5–8.0). Moreover, the combined $(^{208}Pb/^{204}Pb)_i$ ranged from 37.7295 to 37.7851, $(^{207}Pb/^{204}Pb)_i$ ranged from 15.4935 to 15.5037, and $(^{206}Pb/^{204}Pb)_i$ ranged from 17.8910 to 17.9254, indicating that their primitive magma originated from an extremely depleted mantle source with crustal contamination. Integrating this study with regional geology, we propose that the volcanic rocks in the Kebai Fault Zone were most likely formed in a back-arc basin setting induced by ridge subduction.

1. Introduction

Western Junggar has a complex geological evolutionary history and is an important component of the central and southern Central Asian orogenic belt (Chen et al., 2005; Li et al., 2006; Zhu et al., 2007). Magmatic rocks are widely distributed, with evidence of particularly intense volcanic eruptions during the Carboniferous period (Geng et al., 2011; Choulet et al., 2012; Shen et al., 2013; Xu, 2014; Yang et al., 2016; Zhang et al., 2018). Thus, the Early Permian is a crucial period for the tectonic evolution of Western Junggar during the late Paleozoic. The rock assemblage type and degree of development of the Carboniferous volcanic rocks are closely related to the multiple opening and closing processes of the Paleo-Asian Ocean in Western Junggar, offering

---

* Corresponding author.
E-mail address: yzq@xju.edu.cn (Z.-Q. Yao).

Peer review under the responsibility of China University of Petroleum (Beijing).

https://doi.org/10.1016/j.petsci.2025.10.030

clues to the final closing of the residual ocean basin in this region (Dobretsov et al., 1995; Safonova et al., 2017; Kröner et al., 2020). Previous studies have shown that the Late Carboniferous to Early Permian was the ocean–continental transition period in the southern part of Western Junggar. There are three commonly accepted views regarding the tectonic evolution of the region during this period, including an island arc related to subduction (Zhang et al., 2006; Yin et al., 2012; Xiang et al., 2015; Li et al., 2016; Duan et al., 2021), post-collision extension (Han et al., 2006; Su et al., 2006; Li et al., 2024), and ocean ridge subduction (Zhang et al., 2006; Tang et al., 2010, 2012; Yin et al., 2012; Wei et al., 2014; Xiao et al., 2023). However, due to the limited exposure of basement rocks, there is limited understanding of the tectonic evolution of the Junggar Basin prior to deposition. Differing views on the basement attributes of the basin persist (Jiao et al., 2022), hindering further exploration into regional tectonic evolution (Li et al., 2024).

The Kebai Fault Zone is located along the northwestern margin of the Junggar Basin in Xinjiang. The Carboniferous volcanic rock reservoir in this zone was the first discovered in China (Hou, 2012, 2013) and is also one of the main oil-bearing layers in the Junggar Basin. Many exploration wells in the Junggar Basin have obtained industrial oil flow from Carboniferous volcanic rock reservoirs. There are nearly 140 exploration wells with a daily output of more than 10 t of crude oil or 50,000 m^3 of natural gas. They are mainly distributed in the Cheguai and Kebai areas along the northwest margin of the Junggar Basin; Shixi and Luliang areas in the center of the basin; Dixi, Wucaiwan, and Kalamaili areas in the east of the basin; and Beisantai and Xiquan areas in the east of the Junggar Basin (He, 2017). In recent years, the Xinjiang Oilfield Company has utilized three-dimensional seismology to conduct detailed structural interpretations, and based on the re-examination of old wells, they have discovered multiple favorable targets in the Carboniferous strata of the Kebai Fault Zone. Oil tests in wells such as Gu53, Gu16, and Bai861 have achieved industrial oil flow, demonstrating significant potential for oil and gas exploration. Numerous studies have been conducted on various aspects of the Kebai Fault Zone, including its Carboniferous strata, deep volcanic reservoirs, internal structure, lithology, and lithofacies distributions (Dong et al., 2013; Luo et al., 2013; Zhang et al., 2014; Li et al., 2017; Qiu, 2020; Li et al., 2024; Wang et al., 2024). These studies have formed an understanding of the oil and gas accumulation as “full zone with oil, multi-stage with oil” (Kuang, 2007), providing theoretical guidance for the exploration of Carboniferous oil and gas reservoirs in the Kebai Fault Zone. The complex evolutionary processes involved, and our limited understanding of them, warrant comprehensive and detailed analyses of the geodynamic mechanisms of late Paleozoic magmatic activity in Western Junggar and its deep magmatic activity (Xiao et al., 2023).

The eruptive environment of volcanic formations crucially influences reservoir space development (Zhou et al., 2024), which in turn governs the significant differences in space types and physical properties observed across environments (Yu et al., 2004). Thus, zircon U-Pb chronology and isotope geochemistry were selected to study the eruption age, petrogenesis, source region characteristics, and tectonic environment of the Carboniferous volcanic rocks in the Kebai Fault Zone, Western Junggar, Xinjiang, to constrain the tectonic evolution of the late Paleozoic in this region. This work will effectively constrain the spatiotemporal framework of volcanic activity, elucidate the characteristics of magmatic source regions and crust–mantle interactions, provide critical petrological evidence for regional tectonic evolution, and significantly enhance our understanding of geological processes such as subduction and volcanic arc formation, facilitating the accurate prediction of source rocks in Western Junggar.

2. Regional geological background

The Junggar Basin has experienced middle and late Hercynian, Indosinian, Yanshan, and Himalayan tectonic movement since the Late Paleozoic. The Carboniferous and Permian periods were especially important for the formation and evolution of the western basin in northern Xinjiang, marking a significant transition in the sedimentary environment from oceanic to terrestrial conditions. The early Carboniferous extensional rifting environment was impacted by Late Carboniferous residual ocean basin closure, and experienced collisions between the Permian island arcs, blocks, and surrounding plates. This series of events ultimately shaped the present structure of the Junggar Basin, with further changes occurring during the Mesozoic and Cenozoic. The Carboniferous volcanic rocks in Western Junggar are mainly distributed in the Xiemustai-Ser Mountain, Shixi, Beisantai Uplift, Chepaizi Uplift, and Kebai Fault Zone areas (Pan et al., 2022), and belong to the early Carboniferous Songkarsu, Bhatamayineishan, Late Carboniferous Aladeyikesei, Chengjisihanshan, and Hala'alat Formations (Pan et al., 2022). The volcanic rock studied in this research is from the Kebai Fault Zone. Based on lithological associations, the Xinjiang Oilfield Company divided the Carboniferous volcanic rocks of the Kebai Fault Zone into five lithological segments, without specifying stratigraphic assignments (Tang et al., 2012).

The Kebai Fault Zone is located in the western uplift of the Junggar Basin, with a northeast–southwest trend. It is bounded by the Xibaibai Central Fault and the Ninth District of the Northeast Thrust Fault Zone in the northwest, the Kewu Fault in the southeast, and the Da Jurassic Gully and Bailiantan Faults in the southwest. The fault zone generally follows a linear pattern (Fig. 1(a)) (Pan et al., 2022). This zone is a giant nappe frontal fault system composed of multistage overthrust fault stages (Zhou et al., 2023). The Carboniferous volcanic reservoirs are primarily found on the upper plate of the Kebai Fault Zone (Jiang et al., 2013), and the oil-bearing area is contiguous (Fig. 1(b)) (Li et al., 2017). The Mahu Depression is the main hydrocarbon-generating depression in the Kebai Fault Zone (Li, 2008; Li et al., 2017). The strata in the study area are well-developed, with the thickness of the Carboniferous system exceeding 500 m (Liu et al., 2019). Owing to the prolonged geological activity, the stratigraphic development of the upper and lower walls of the Kebai Fault is markedly different. The contacts between the Carboniferous strata and the overlying Jurassic and Triassic strata are angular unconformities. The overlying Permian strata are only locally developed and exhibit limited unconformity contacts with the Carboniferous, whereas the Jurassic strata above have widespread contacts with the Carboniferous. The strata at the top interface of the Carboniferous system are characterized by strong amplitude reflection in the seismic section, which is easy to distinguish. The contact between the inner strata and top surface is also an angular unconformity, and the inner strata exhibit clear imaging, good continuity, and traceability. However, based on the analysis of available well data, it is difficult to interpret the drilled Carboniferous reservoir using a stratification method parallel to the top of the Carboniferous system, particularly at the depth of the inner strata (Fig. 1(c)).

3. Sampling and analysis methods

Samples were collected from four drilling cores in the Kebai Fault Zone, of which 15 geochemical samples comprised mainly andesite. The SHRIMP zircon U-Pb isotope dating sample was crystalline tuff (BW28), and the laser ablation inductively coupled plasma mass spectrometry (LA-ICP-MS) zircon U-Pb isotope dating sample was andesite (G54-8).

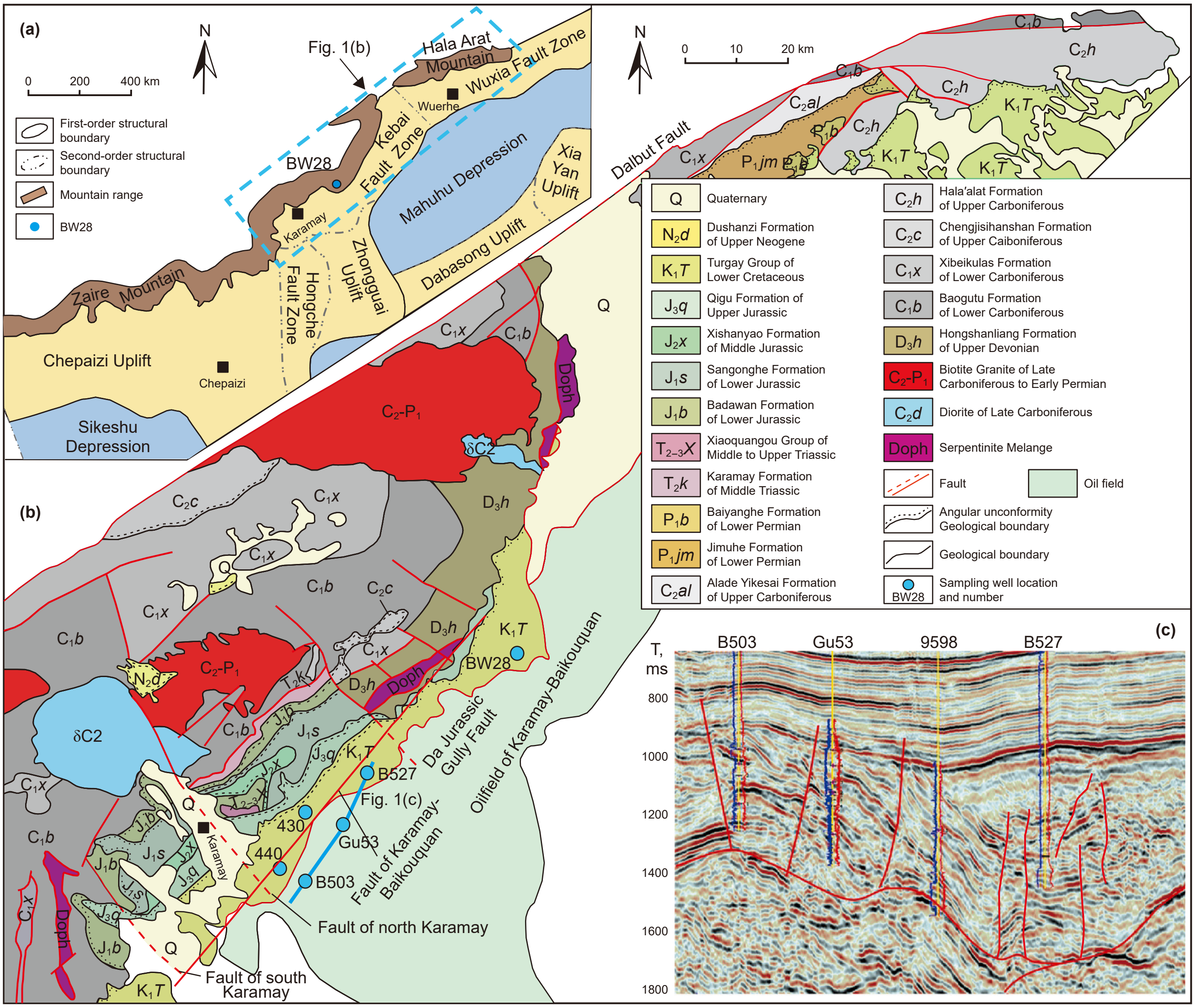

Fig. 1. **(a)** Structural location of the study area, **(b)** schematic map of Karamay-Baikouquan area, and **(c)** seismic profile through B527 (according to Wang et al. (2024)).

3.1. Sample collection

Andesite exhibits porphyritic and massive textures, with variations in mineral composition and structure across different samples. Fig. 2(a) and (b), show porphyritic and massive textures, where the porphyry consists of plagioclase and minor hornblende, and the matrix features a glassy interwoven structure composed of microcrystalline and cryptocrystalline plagioclase, with secondary opaque metallic minerals (mostly magnetite). In Fig. 2(c) and (d), the rock exhibits porphyritic and massive textures. The phenocrysts consist primarily of plagioclase, hornblende, and biotite; the matrix has an interwoven texture of microcrystalline plagioclase, hornblende, diopside, and trace quartz. This is accompanied by opaque metallic minerals and extensive secondary alterations including claying and epidotization. In Fig. 2(e) and (f), the andesite presents a porphyritic texture with a weakly oriented structure, where the phenocrysts are mainly feldspar and the matrix has an intergranular structure of plagioclase, quartz, and chlorite, with accessory opaque metallic phases and extensive development of chlorite and sericite.

The crystalline tuff shows a crystalline tuffaceous structure (Fig. 2(g) and (h)) and a massive texture. Composed of crystal fragments, rock fragments, and minor volcanic glass fragments, with opaque metallic accessory minerals, this rock has undergone extensive alteration, dominated by sericitization and clayification.

3.2. Test and analysis methods

Sample processing was conducted by Langfang Yuhongyan Mineral Science and Technology Co., Ltd. Whole-rock sample major elements and trace element composition, and Sr-Nd-Pb isotope testing were completed by Wuhan Sample Solution Analytical Technology Co., Ltd. The SHRIMP zircon U-Pb isotope testing was carried out at the Beijing Ion Probe Center of the Chinese Academy of Geological Sciences. LA-ICP-MS zircon U-Pb isotope testing was performed at the Institute of Geomechanics of the Chinese Academy of Geological Sciences.

The major element analysis was performed using a ZSXPrimus II wavelength dispersion X-ray fluorescence spectrometer (Rigaku, Japan). The standard curve was based on the national standard material rock series GBW07101-14, and the theoretical α

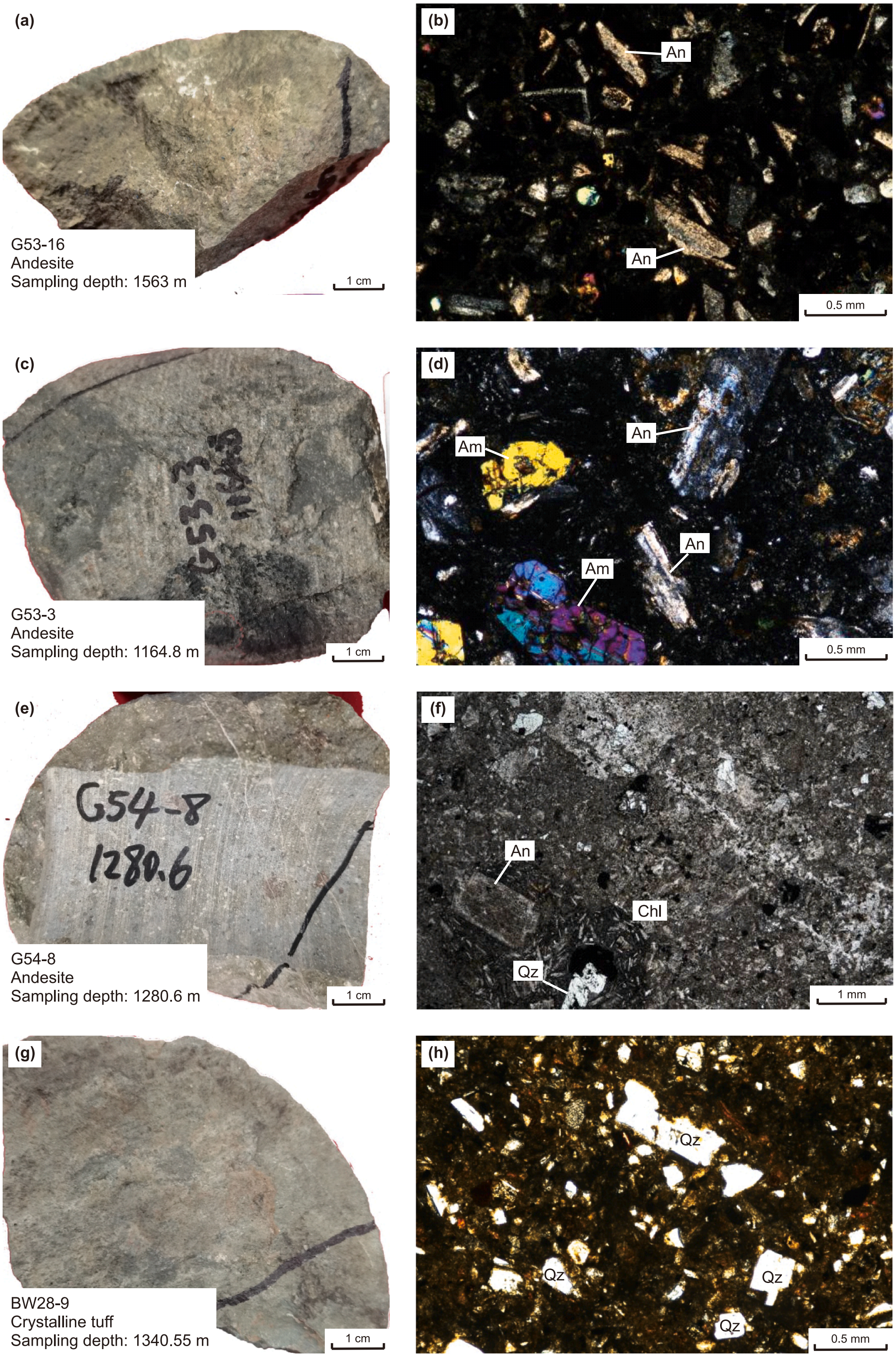

QZ: Quartz; An: Anorthose; Am: Amphibole; Chl: Chlorite

Fig. 2. Macro and micro photos of volcanic rock samples.

coefficient method was used for data correction, with a test relative standard deviation of <2%. The trace element content was determined using an Agilent 7700e inductively coupled plasma mass spectrometer (ICP-MS). For this, samples sieved through 200 mesh were dried in an oven at 105 °C for 12 h. The powder sample (50 mg) was placed in a Teflon sample digestion bomb, and 1 mL high-purity HNO_3 and 1 mL high-purity HF were slowly added in sequence. The Teflon sample digestion bomb was placed into a steel sleeve, tightened, and then heated in an oven at 190 °C for more than 24 h. After cooling, the digestion bomb was opened and placed on an electric heating plate at 140 °C for evaporative drying. Then, 1 mL HNO_3 was added and evaporated again. Next, 1 mL high-purity HNO_3, 1 mL MQ water, and 1 mL internal standard (concentration of 1 ppm) were added, and the Teflon sample digestion bomb was placed back into the steel sleeve, tightened, and heated in an oven at 190 °C for more than 12 h. Finally, the solution was transferred into a polyethylene bottle and diluted to 100 g with 2% HNO_3 for ICP-MS testing.

The whole-rock Sr-Nd-Pb isotope ratio analysis was conducted using a multi-collector ICP-MS (NeptunePlus) instrument from ThermoFisher Scientific (Germany). For the Sr isotope analysis, samples were analyzed by inserting seven samples between two Sr isotope standards (NIST987 and AlfaSr), with BCR-2 (basalt) and RGM-2 (rhyolite) (United States Geological Survey) chosen as the process-monitoring samples. The actual sample test internal precision = 0.000010–0.000020 (approximately 0.01‰–0.03‰, 2RSE), with an accuracy better than 0.000020 (~0.03‰). For the Nd isotope analysis, samples were analyzed by inserting seven samples between two Nd isotope standards (GSB 04-3258-2015 and AlfaNd), with BCR-2 (basalt) and RGM-2 (rhyolite) (United States Geological Survey) chosen as the process-monitoring samples. The sample test precision = 0.000005–0.000025 (approximately 0.01‰–0.05‰, 2RSE), and the test accuracy was better than 0.000025 (~0.05‰). For the Pb isotope analysis, samples were analyzed by inserting seven samples between two Pb isotope standards (NIST981 and AlfaPb), with BCR-2 (basalt) chosen as the process-monitoring sample. The $^{208}Pb/^{204}Pb$ test internal precision (2RSE) was 0.002%–0.025%, and the test accuracy was better than 0.03%. The data were processed using the professional isotope data processing software “Iso-Compass”.

The SHRIMP zircon U-Pb dating protocol employed conventional flotation and electromagnetic separation methods for sorting, followed by selecting zircon grains with intact crystal forms under a binocular microscope, and mounting them alongside standard zircon (TEM) on the surface of epoxy resin. After polishing, they were transformed into sample targets at the Beijing Ion Probe Center. The zircons to be tested underwent transmitted light, reflected light photography and cathodoluminescence imaging to study their growth characteristics. Locations without fractures or inclusions, and with uniform cathodoluminescence images were chosen for calibration. Then, after cleaning and gold-plating the sample targets, measurements were conducted on a SHRIMP II ion probe instrument, according to standard laboratory procedures. The standard samples M257 ($U = 840 \times 10^{-6}$) and TEM (age: 417 Ma) were used for zircon U content and age correction, respectively. The SQUID and ISOPLOT programs were used for data processing. The common lead was corrected based on the measured ^{204}Pb content, with the isotope ratios and single-point age errors both being 1σ, and the weighted average age error being within the 95% confidence interval. The SHRIMP zircon U-Pb dating method, experimental analysis, and data processing procedures are detailed in relevant literature (Williams, 1998; Song et al., 2002; Wu et al., 2024). The SQUID1.02 (Ludwig, 2003) and ISOPLOT3.0 programs (Ludwig, 2003) were adopted for the sample data and graphical processing, respectively.

The LA-ICP-MS zircon U-Pb isotope tests were conducted using the PQ-MS ICP-MS from Analytik Jena and the NWR193 nm high-energy ArF laser from ESL, equipped with a TV3 ablation cell. During the laser ablation process, helium and argon gasses was used as the carrier and compensation gasses, respectively, to adjust the sensitivity; they were mixed through a T-junction before entering the ICP. The laser ablation system was equipped with a signal smoothing device. The laser beam spot and frequency of this analysis were 30 μm and 5 Hz, respectively. The zircon standard 91500 and glass standard NIST610 were used as external standards for isotope and trace element fractionation correction in U-Pb isotope dating and trace element content processing. Each time-resolved analysis dataset included about 20–30 s of blank signal and 40 s of sample signal. Offline processing of the analysis data (including the selection of samples and blank signals, correction of instrument sensitivity drift, and calculation of the element content, U-Pb isotope ratio, and age) was completed using the software iolite 4. During the experiment, for every 10 sample points tested, two standard points and one monitoring point were tested, ensuring that each batch of experiments started and ended with two controlled standard points. The drawing of the zircon sample U-Pb age harmonic diagrams and the calculation of the age-weighted average were completed using Isoplot/Ex_ver3 (Ludwig, 2003).

4. Results

4.1. Major elements

The major, trace, and rare earth element analysis results of 15 volcanic rock samples from four drilling cores in the Kebai Fault Zone are shown in Table 1. Overall, the samples had moderate loss on ignition (LOI) values (1.85%–4.32%), indicating that late weathering has had an influence on the rock samples. Some of the LOI values were relatively large, such as that of the B80-4 sample with strong epidotization, nazoisite, and chlorite, where the LOI value reached 7.14 wt%, indicating a difference in late weathering. This may have introduced some deviations into the rock series, magma source characteristics, and tectonic environment. In the subsequent text, low-activity element ratios (such as Th/Yb vs. Nb/Yb) are adopted to assist in discriminating the tectonic environment (Pearce, 2008). By combining isotopes ($\varepsilon_{Nd}(t)$) and trace elements (such as Nb/La) to constrain the source area, and avoiding reliance on a single major element indicator, interference in the interpretation of the genesis and tectonic environment of these samples can be effectively reduced (Pearce, 1984).

The SiO_2 content of the current samples ranged from 53.46 to 61.57 wt%, with an average of 58.03 wt%; the TiO_2 content was 0.75–1.20 wt% (average 0.86 wt%); and the Al_2O_3 content was 14.85–19.41 wt% (average 17.39 wt%), which is similar to that of continental overflow basalt (Al_2O_3 = 17.08 wt%) (Xia and Li, 2019). The MgO content ranged from 1.30 to 4.85 wt%, the total alkali content ($Na_2O + K_2O$) was 5.25–8.24 wt% (average 6.58 wt%), the Na_2O content was 3.54–6.78 wt% (average 5.28 wt%), and the K_2O content was 0.46–2.35 wt% (average 1.29 wt%).

4.2. Rare earth elements and trace elements

The total amount of rare earth elements ($\sum$REE) in the volcanic rocks of these samples was 31.59×10^{-6} to 214.13×10^{-6}, the total amount of light rare earth elements ($\sum$LREE) was 23.81×10^{-6} to 160.26×10^{-6}, and the total amount of heavy rare earth elements ($\sum$HREE) was 7.70×10^{-6} to 53.87×10^{-6}. The $\sum$LREE/$\sum$HREE values ranged from 2.97×10^{-6} to 5.39×10^{-6}, with an average of

Table 1
Analysis results of major elements (wt%), trace elements (ppm) and rare earth elements (ppm) of Andesite in Late Carboniferous volcanic rocks in Kebai Fault Zone.

Sample	G53-1	G53-2	G53-6	G53-7	G53-8	G53-9	G53-12	G53-15	G53-16	G53-3	G53-4	G53-11	440–1	B80-4	BW22-5
SiO_2	59.95	56.72	59.20	55.02	53.46	59.05	59.75	59.81	57.16	54.79	56.34	56.88	59.48	61.23	61.57
TiO_2	0.87	0.75	0.85	0.85	0.87	0.81	0.94	0.80	0.79	0.80	0.77	0.87	1.20	0.81	0.87
Al_2O_3	16.44	18.14	16.74	17.43	17.42	17.04	16.34	17.70	17.41	19.41	18.51	18.26	16.50	14.85	18.66
Fe_2O_3	7.65	7.88	7.07	8.36	8.68	8.72	8.01	8.57	8.62	8.00	7.63	8.66	9.95	6.68	7.18
MnO	0.12	0.09	0.14	0.17	0.18	0.16	0.12	0.11	0.11	0.13	0.11	0.16	0.20	0.19	0.10
MgO	3.87	3.55	4.12	4.60	4.85	4.78	3.89	3.71	3.82	4.19	3.84	4.52	3.12	3.36	1.30
CaO	2.60	6.38	4.34	8.10	9.13	3.11	2.64	1.55	5.16	6.52	6.93	4.26	2.56	6.79	3.44
Na_2O	6.78	5.18	5.71	4.82	4.79	4.62	6.40	6.68	5.80	5.21	4.92	4.74	5.56	3.54	4.51
K_2O	1.56	1.19	1.69	0.50	0.46	1.59	1.73	0.94	1.00	0.83	0.82	1.52	1.02	2.35	2.22
P_2O_5	0.16	0.11	0.15	0.15	0.15	0.12	0.17	0.12	0.14	0.13	0.12	0.13	0.41	0.19	0.17
LOI	3.06	2.23	3.58	3.55	4.32	3.79	2.82	2.93	1.92	1.85	2.21	4.20	3.06	7.14	2.97
$Na_2O + K_2O$	8.34	6.37	7.40	5.32	5.25	6.20	8.13	7.62	6.80	6.04	5.75	6.26	6.58	5.88	6.73
FeO	6.88	7.09	6.36	7.52	7.81	7.85	7.21	7.71	7.76	7.20	6.87	7.80	8.95	6.01	6.46
FeO/MgO	1.78	2.00	1.54	1.64	1.61	1.64	1.85	2.08	2.03	1.72	1.79	1.72	2.87	1.79	4.98
σ	4.11	2.96	3.38	2.36	2.64	2.40	3.95	3.46	3.27	3.10	2.48	2.82	2.63	1.90	2.44
Li	9.58	14.12	25.32	17.18	18.52	12.96	11.52	15.19	12.55	12.18	12.69	12.89	19.89	13.38	46.17
Be	0.55	0.48	0.48	0.47	0.44	0.50	0.57	0.86	0.59	0.47	0.44	0.58	1.45	0.79	1.19
Sc	19.04	20.07	19.61	21.31	21.78	19.34	23.02	21.92	20.08	18.03	18.53	19.30	24.04	18.81	18.10
V	159.16	191.02	158.81	187.52	189.48	165.20	178.19	181.64	170.09	238.04	194.09	183.15	12.84	154.64	187.52
Cr	46.76	25.25	52.71	63.86	65.72	45.67	48.39	57.31	41.15	26.55	24.43	43.85	0.67	46.46	15.77
Co	19.61	19.57	18.20	22.06	23.44	21.01	20.60	23.57	21.82	20.02	18.61	21.90	7.83	13.07	9.22
Ni	34.06	15.23	31.85	34.21	34.90	28.77	32.92	33.67	29.09	17.55	16.87	34.27	0.86	17.28	19.17
Cu	65.82	24.48	36.82	28.60	25.95	74.89	79.39	72.83	70.52	15.30	17.62	78.28	16.62	81.08	42.41
Zn	68.36	71.93	64.08	76.92	80.47	73.41	70.40	69.30	71.25	81.39	69.34	83.90	141.04	69.77	257.63
Ga	15.66	19.65	16.48	20.11	20.72	19.98	16.89	17.91	18.34	22.52	22.02	19.89	22.03	15.90	22.31
Rb	15.62	16.43	28.76	7.33	7.51	23.68	17.99	13.33	14.21	11.64	12.59	22.30	19.71	32.81	51.12
Sr	373.86	532.55	391.50	428.80	431.84	364.25	432.98	465.58	463.66	515.38	490.80	387.68	545.64	228.92	424.68
Y	20.69	11.16	18.66	19.71	19.74	14.16	22.89	11.54	15.18	11.25	11.08	18.28	76.25	23.74	23.02
Zr	103.17	46.47	87.54	89.90	90.19	80.56	112.88	39.62	64.81	47.09	46.82	81.68	326.12	147.90	147.38
Nb	1.80	0.71	1.49	1.39	1.44	1.75	1.89	1.05	1.18	0.77	0.74	1.77	8.37	3.83	5.02
Sn	0.86	0.49	0.77	0.82	0.77	0.77	0.90	0.65	0.83	0.47	0.59	0.83	2.68	1.07	1.58
Cs	0.65	0.30	0.42	0.22	0.18	0.38	0.22	0.12	0.39	0.22	0.30	0.70	0.10	0.90	1.13
Ba	435.10	260.26	346.53	168.30	160.59	287.21	443.07	217.44	222.48	234.31	213.64	311.01	342.36	678.60	469.00
La	7.04	3.70	5.74	5.87	5.97	6.64	7.60	6.53	5.28	3.97	3.85	7.63	22.81	14.29	16.49
Ce	18.06	9.23	14.35	14.63	14.82	14.95	19.52	15.14	12.37	9.63	9.27	18.29	63.32	32.79	36.96
Pr	2.66	1.50	2.29	2.34	2.37	2.28	2.86	1.92	1.94	1.51	1.47	2.51	10.39	4.44	5.34
Nd	11.56	6.76	10.51	10.54	10.48	9.50	12.73	9.34	9.16	7.11	6.67	10.82	47.49	17.86	21.44
Sm	3.23	1.91	2.98	3.06	3.02	2.58	3.74	2.34	2.58	2.06	1.99	3.02	13.52	4.22	5.48
Eu	0.89	0.71	0.82	0.88	0.89	0.84	0.97	0.75	0.82	0.71	0.70	0.87	2.72	1.09	0.85
Gd	3.38	2.09	3.02	3.12	3.18	2.63	3.64	2.33	2.60	2.03	2.02	3.00	13.61	3.94	4.78
Tb	0.59	0.34	0.54	0.54	0.55	0.43	0.64	0.38	0.46	0.35	0.35	0.52	2.40	0.66	0.80
Dy	3.72	2.19	3.40	3.58	3.48	2.87	4.15	2.25	3.01	2.23	2.21	3.36	15.41	4.20	4.59
Ho	0.76	0.43	0.67	0.69	0.72	0.56	0.82	0.45	0.58	0.43	0.41	0.66	3.01	0.82	0.83
Er	2.11	1.23	1.96	2.07	2.03	1.65	2.35	1.25	1.70	1.27	1.22	1.86	8.55	2.45	2.31
Tm	0.30	0.17	0.28	0.29	0.29	0.25	0.33	0.18	0.24	0.18	0.18	0.27	1.29	0.36	0.32
Yb	1.98	1.16	1.80	1.95	1.96	1.62	2.20	1.09	1.60	1.14	1.14	1.76	8.37	2.43	2.09
Lu	0.30	0.17	0.27	0.29	0.29	0.25	0.32	0.16	0.24	0.17	0.17	0.27	1.24	0.38	0.31
Hf	3.14	1.51	2.71	2.84	2.79	2.49	3.59	1.93	2.06	1.57	1.51	2.50	9.32	4.26	4.33
Ta	0.13	0.05	0.11	0.10	0.10	0.12	0.14	0.07	0.08	0.05	0.05	0.13	0.55	0.25	0.34
Tl	0.07	0.06	0.07	0.02	0.03	0.06	0.07	0.03	0.04	0.04	0.03	0.07	0.06	0.10	0.12
Pb	4.43	3.67	2.46	3.20	3.12	4.58	4.42	3.14	4.85	3.34	3.06	6.42	4.73	5.97	7.97
Th	1.83	0.71	1.55	1.57	1.63	1.57	2.03	0.97	1.12	0.71	0.70	1.56	3.71	4.05	4.16
U	0.64	0.24	0.49	0.51	0.51	0.50	0.64	0.18	0.33	0.23	0.25	0.48	1.17	1.06	1.55
Zr/TiO_2	0.01	0.01	0.01	0.01	0.01	0.01	0.01	0.00	0.01	0.01	0.01	0.01	0.03	0.02	0.02
Nb/Y	0.09	0.06	0.08	0.07	0.07	0.12	0.08	0.09	0.08	0.07	0.07	0.10	0.11	0.16	0.22
Nb/Yb	0.91	0.61	0.83	0.71	0.73	1.08	0.86	0.96	0.74	0.67	0.65	1.01	1.00	1.58	2.40
Th/Yb	0.92	0.61	0.86	0.81	0.83	0.97	0.92	0.89	0.70	0.62	0.61	0.89	0.44	1.67	1.99
Rb/Sr	0.04	0.03	0.07	0.02	0.02	0.07	0.04	0.03	0.03	0.02	0.03	0.06	0.04	0.14	0.12
Ti/1000	5.20	4.50	5.10	5.09	5.19	4.83	5.64	4.81	4.73	4.77	4.59	5.20	7.17	4.88	5.21
V	159.16	191.02	158.81	187.52	189.48	165.20	178.19	181.64	170.09	238.04	194.09	183.15	12.84	154.64	187.52
$\sum$REE	56.58	31.59	48.64	49.86	50.06	47.06	61.88	44.11	42.58	32.82	31.65	54.82	214.13	89.93	102.62
$\sum$LREE	43.44	23.81	36.70	37.33	37.56	36.79	47.42	36.03	32.15	25.01	23.95	43.14	160.26	74.70	86.57
$\sum$HREE	13.14	7.77	11.94	12.53	12.50	10.27	14.46	8.09	10.43	7.82	7.70	11.68	53.87	15.24	16.05
$\sum L/\sum H$	3.31	3.06	3.07	2.98	3.00	3.58	3.28	4.46	3.08	3.20	3.11	3.69	2.97	4.90	5.39
δEu	0.27	0.35	0.27	0.28	0.29	0.32	0.26	0.32	0.32	0.35	0.35	0.29	0.20	0.27	0.17

Note: $\delta Eu = 2 \times Eu_N/(Sm_N + Gd_N)$, where N is the standardized value of chondrites, quoted from Sun and McDonough (1989); $\sigma = (Na_2O\ (wt\%) + K_2O\ (wt\%))^2/(SiO_2\ (wt\%) - 43)$; The data in the table and the text are the data of re-differentiation after the loss of combustion is removed. Initial arc basalt according to Wang et al. (2021); Arc volcanic rocks of Hala'alat Formation (307–303 Ma) according to Xiang et al. (2015), Li et al. (2017); Adakite of Hala'alat Formation according to Jiang et al. (2023).

3.54×10^{-6}, indicating a slight difference. The total δEu values of the rocks were 0.17–0.35, showing a weak negative Eu anomaly (Fig. 4(a)). The $(La/Yb)_N$ values ranged from 2.72 to 7.89, with an average of 4.03, indicating that the samples belong to the light-rich rare earth type. The $(La/Sm)_N$ values ranged from 1.69 to 3.38, with an average of 2.26. The degree of internal fractionation in the

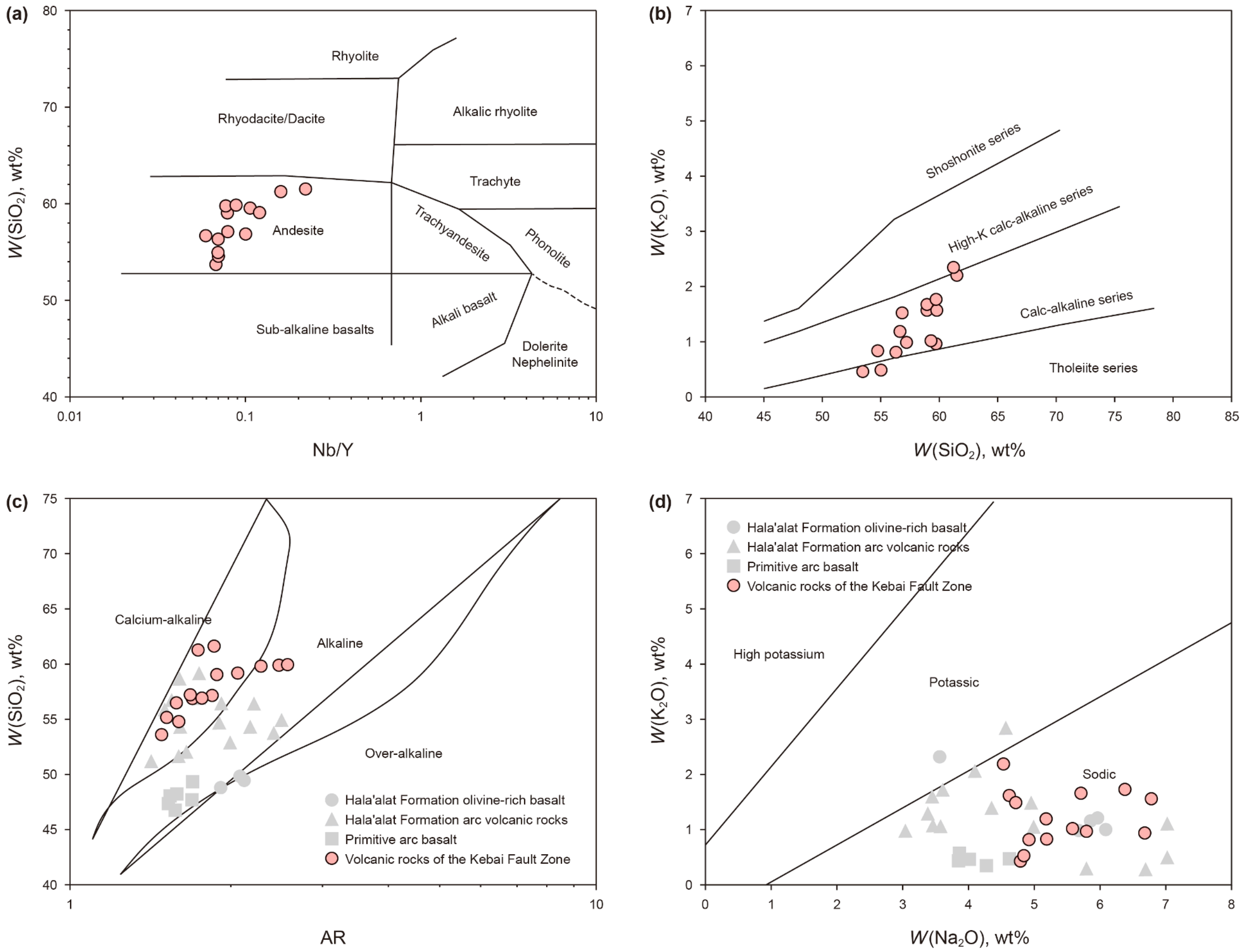

Fig. 3. **(a)** SiO_2-Nb/Y of Kebai Fault Zone andesite (according to Winchester and Floyd (1977)), **(b)** SiO_2-K_2O (according to Peccerillo and Taylor (1976)), **(c)** AR-SiO_2 (according to Wright (1969)) and **(d)** Na_2O-K_2O (according to Middlemost (1972)). The data of rich porphyry basalt, arc volcanic rock and initial arc basalt of Hala'alat Formation were obtained from Li et al. (2024).

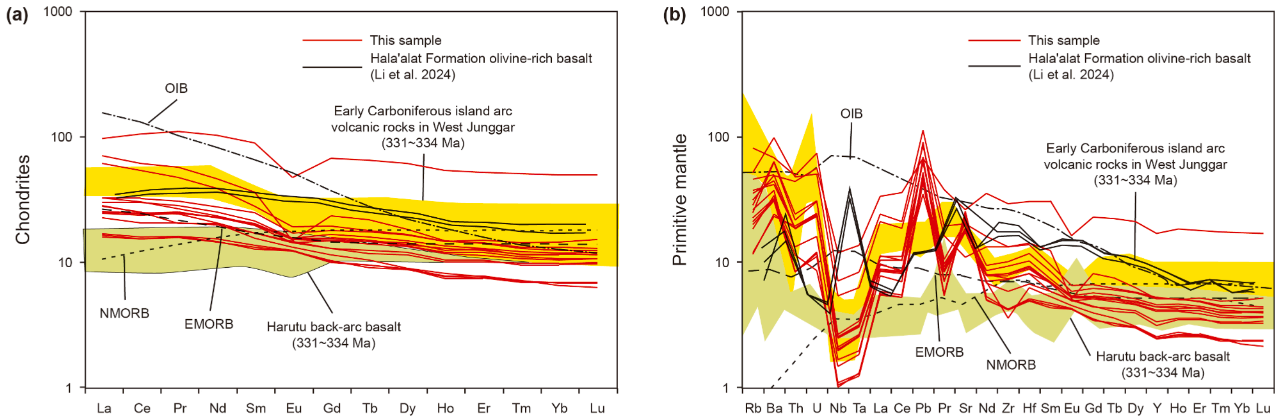

Fig. 4. **(a)** Standardized rare earth element partitioning diagram of volcanic chondrites in Kebai Fault Zone and **(b)** standardized trace element cobweb diagram of primitive mantle (modified from Xiao et al. (2023)).

heavy rare earth elements was low ($(Gd/Yb)_N = 1.70$ to 2.29, average 1.75). In the standardized curve diagram of chondrites (Fig. 4(a)), the partition curve was consistent with a slightly right-leaning pattern, showing the relative enrichment of light rare earth elements and the relative loss of heavy rare earth elements. The differentiation between the light and heavy rare earth elements was obvious. The spider diagram of the normalized trace elements in the original mantle (Fig. 4(b)) shows that large ion lithophilic elements, such as Ba, Th, U, and Sr, are relatively enriched, while high-field strength elements, such as Nb, Ta, Zr, and Hf, are relatively depleted, which is typical of island arc volcanic rocks.

4.3. Zircon U-Pb chronology

Zircons were selected from the crystalline tuffs (BW28, 1257.3–1257.7 m) and almond andesite (G54-8, 1280.6 m) collected from the cores of two boreholes, BW28 and G54, and SHRIMP and LA-ICP-MS zircon U-Pb dating studies were conducted.

The Th content of the 20 effective points of the tuff samples ranged from 42.44 × 10^{-6} to 474.44 × 10^{-6}, the U content ranged from 107.29 × 10^{-6} to 431.16 × 10^{-6}, and the Th/U value of the zircons ranged from 0.41 to 1.14, showing a strong positive correlation (Table 2). This suggests typical magmatic zircons (Hoskin and Black, 2010). The age of the $^{206}Pb/^{238}U$ sample ranged from 287.0 to 421.8 Ma, with a maximum age error of 5.2 Ma. The 20 data points were clustered around the harmonic curve (Fig. 5(a)), and the weighted average age of $^{206}Pb/^{238}U$ was 316.8 ± 1.7 Ma (Mean Squared Weighted Deviation = 1.15), representing the eruption age.

The andesite samples (from 51 sites) with a concordance degree greater than 90% had Th contents ranging from 24.60 × 10^{-6} to 1295.70 × 10^{-6}, U contents ranging from 45.32 × 10^{-6} to 627.89 × $10^{-6,}$ and zircon Th/U values ranging from 0.39 to 1.87, showing a positive correlation (Table 2). This also indicates typical magmatic zircons (Hoskin and Black, 2010). The age of the $^{206}Pb/^{238}U$ was 289.44–349.42 Ma, and the maximum age error was 28.60 Ma. The data points were clustered around the harmonic curve (Fig. 5(b)), and the weighted mean age of $^{206}Pb/^{238}U$ was 321.7 ± 2.5 Ma (Mean Squared Weighted Deviation = 2.7), representing the eruption age.

4.4. Sr-Nd-Pb isotopes

The Sr, Nd, and Pb isotope analyses were performed on six volcanic rock samples and the results are shown in Table 3. $^{87}Sr/^{86}Sr$ ranged from 0.703927 to 0.705671, $^{147}Sm/^{144}Nd$ ranged from 0.15727 to 0.18037, $^{208}Pb/^{204}Pb$ ranged from 37.8520 to 38.1960, $^{207}Pb/^{204}Pb$ ranged from 15.5010 to 15.5270, and $^{206}Pb/^{204}Pb$ ranged from 18.0670 to 18.3400. The initial isotope ratio correction at 316 Ma showed that $(^{87}Sr/^{86}Sr)_i$ was 0.703941–0.705675, $(^{143}Nd/^{144}Nd)_i$ was 0.512232, $\varepsilon_{Nd}(t)$ was 7.5–8.0, and the two-stage model age T_{2DM} was 429–469 Ma. $(^{208}Pb/^{204}Pb)_i$ ranged from 37.7295 to 37.7851, $(^{207}Pb/^{204}Pb)_i$ ranged from 15.4935 to 15.5037, and $(^{206}Pb/^{204}Pb)_i$ ranged from 17.8910 to 17.9254.

The volcanic rock samples showed low $(^{87}Sr/^{86}Sr)_i$ values (0.703941–0.705675) and positive $\varepsilon_{Nd}(t)$ values (7.5–8.0). In the Sr–Nd isotope diagram (Fig. 6(a) and (b)), four of the six samples fell within the Early Carboniferous island arc volcanic rocks of Western Junggar. $(^{87}Sr/^{86}Sr)_i$–$(^{143}Nd/^{144}Nd)_i$, $(^{206}Pb/^{204}Pb)_i$–$(^{207}Pb/^{204}Pb)_i$, $(^{206}Pb/^{204}Pb)_i$–$(^{208}Pb/^{204}Pb)_i$ (Fig. 6(c), (d), (e), (f)) almost all fell near the mantle line, indicating that the samples have similar affinities to the mantle and may have similar magmatic sources.

5. Discussion

5.1. Eruption age

The Carboniferous volcanic rocks in the Junggar area are characterized by multi-stage eruptions, diverse lithologies, multiple eruption centers, and complex compositions (Zhang, 2020), Their eruptions are mainly concentrated at 300–310 Ma, 310–320 Ma, and 320–330 Ma (Fig. 7, Table 4), providing a basis for regional volcanic activity and stratigraphic comparison. These age groups roughly correspond to the Hala'alat, Chengjisihanshan, and Xibeikulas Formations. Because the volcanic rocks are not exposed, there are few paleontological fossils in core samples, and the stratigraphic ages inferred from paleontological data are inconsistent with the chronology of the volcanic rocks (Wang et al., 2007; Guo et al., 2010), resulting in poorly constrained stratigraphic assignments and eruption ages. The Xinjiang Oilfield Company divided the Carboniferous volcanic rocks in the study area into five lithologic units based on lithological associations, which hinders regional stratigraphic correlation. For example, Xiang et al. (2013) assigned samples from the north bank of the Darbut River and Hongshan pluton in the West Karahuka area, with LA-ICP-MS zircon U-Pb ages of 312 ± 19 Ma (andesite) and 312 ± 13 Ma (basalt) to the Chengjisihanshan Formation. This classification relied on lithofacies associations, fossil evidence, and regional stratigraphic correlations, suggesting a Late Carboniferous origin. Regionally, angular unconformities separate the Lower Carboniferous Tubao–Gutu and Xibeikulas Formations from overlying strata (Xiang et al., 2013). The Chengjisihanshan Formation is characterized by interbedded pyroclastic rocks (e.g., volcanic lava) and normal sedimentary fine-to-coarse clastic rocks, including tuffaceous lithic siltstone, andesitic lithic tuffaceous sandstone interbedded with mudstone, basaltic tuffaceous lithic sandstone, gravel-bearing lithic sandstone, purplish-red medium-fine conglomerate, purplish-red argillaceous siltstone, cataclastic basaltic andesite, grey-black vesicular-almond basalt, and grey volcanic breccia agglomerates. Fossil assemblages include *Choristites* sp., *Pseudotimania* sp., and corals.

In boreholes BW28 and G54, the core lithology is lithic crystalline tuff and almond andesite (Fig. 2(e), (f), (g), (h)). The U-Pb harmonic age of the tuff zircon (SHRIMP) is 316.8 ± 1.7 Ma, and the U-Pb harmonic age of the andesite zircon (LA-ICP-MS) is 321.7 ± 1.8 Ma. This represents the Late Carboniferous volcanic eruption age and can be compared with that of the Chengjisihanshan Formation reported by Xiang et al. (2013).

5.2. Petrogenesis and magmatic source

The volcanic rocks of the Kebai Fault Zone are intermediate-acidic calcareous alkaline magmatic rocks with a moderate MgO content (1.30–4.85 wt%) and a SiO_2 content ranging from 53.46% to 61.57%, with an average of 58.03%. The volcanic rocks in island arcs are mainly formed by the dehydration of subduction plates to form a fluid metasomatism mantle wedge rich in large ion lithophile elements, which are then partially melted, resulting in volcanic rocks with some distinctive geochemical characteristics. Notably, these rocks are enriched in large ion lithophile elements, while exhibiting a depletion in high field strength elements (Tatsumi and Kogiso, 2003). The magma reflects the partial melting of a water-rich mantle wedge, which may originate from subduction fluid alteration. Unlike the high MgO content (6–9 wt%, with prominent high-magnesium characteristics) of the high-magnesium diorites in Southern Junggar (Pan et al., 2022), which may imply a direct reaction between magma and mantle peridotite (such as slab melt interacting with the mantle). Therefore, the bimodal volcanic rocks in Eastern Junggar are more consistent with a crustal stretching–mantle upwelling mechanism under rift or post-collision extensional environments. The standardized rare earth element partition map of chondrites (Fig. 4(a)) shows that the volcanic rocks in the Kebai Fault Zone are enriched in light rare earth elements, and the light and heavy rare earth elements are clearly differentiated. The large ion lithophilic elements, such as Ba, Th, U, and Sr, are relatively enriched, while the high field strength elements, such as Nb, Ta, Zr, and Hf, are relatively depleted (Fig. 4(b)), which is typical of island arc magma origins. The significant Nb-Ta depletion (Nb/La = 0.16–0.30) and large ion

Table 2
SHRIMP and LA-ICP-MS zircon U-Pb isotopic dating results of Late Carboniferous tuff in Kebai Fault Zone.

Spot	Element content, ppm			$^{232}Th/^{238}U$	Isotope ratio						Age and error					
	Pb	Th	U		$^{207}Pb/^{206}Pb$	±%	$^{207}Pb/^{235}U$	±%	$^{206}Pb/^{238}U$	±%	$^{207}Pb/^{206}Pb$	σ	$^{206}Pb/^{238}U$	σ	$^{208}Pb/^{232}Th$	σ
BW28 SHRIMP zircon U-Pb																
BW28-1	6.30	42.00	107.00	0.41	0.052	7.9	0.487	8.0	0.068	1.3	294	±180	421.8	±5.2	374	±34
BW28-2	7.29	129.00	175.00	0.76	0.050	5.3	0.332	5.6	0.048	1.6	194	±120	303.4	±4.8	279	±10
BW28-3	9.07	122.00	210.00	0.60	0.051	3.8	0.352	3.9	0.050	1.0	235	±87	316.1	±3.2	314.9	±9.2
BW28-4	5.96	63.00	141.00	0.46	0.051	6.3	0.345	6.4	0.049	1.2	252	±140	307.2	±3.5	280	±16
BW28-5	11.00	212.00	279.00	0.79	0.049	5.1	0.309	5.2	0.046	1.0	161	±120	287	±2.8	279	±14
BW28-6	10.70	143.00	247.00	0.60	0.054	2.7	0.373	2.9	0.051	1.0	352	±61	317.6	±3.0	321.1	±7.1
BW28-7	8.34	88.00	190.00	0.48	0.052	4.5	0.362	4.6	0.051	1.1	264	±100	320.8	±3.4	316	±13
BW28-8	7.15	94.00	166.00	0.59	0.053	5.7	0.364	5.8	0.050	1.1	317	±130	314.7	±3.5	313	±14
BW28-9	8.58	87.00	194.00	0.46	0.052	3.0	0.369	3.2	0.051	1.1	289	±69	322.8	±3.3	312.4	±8.9
BW28-10	12.00	175.00	278.00	0.65	0.054	2.3	0.371	2.5	0.050	1.0	360	±52	315.4	±3.0	317.2	±6.2
BW28-11	15.20	320.00	361.00	0.92	0.052	3.0	0.350	3.2	0.049	0.9	283	±69	307.4	±2.8	301.4	±6.4
BW28-12	12.30	178.00	287.00	0.64	0.053	3.0	0.361	3.2	0.050	1.0	315	±68	313.1	±2.9	305.7	±7.2
BW28-13	9.02	127.00	210.00	0.62	0.053	4.6	0.366	4.7	0.050	1.1	321	±100	315.9	±3.3	334	±11
BW28-14	15.10	258.00	361.00	0.74	0.053	2.3	0.353	2.5	0.049	0.9	313	±53	306.4	±2.8	313	±7.1
BW28-15	7.75	144.00	178.00	0.83	0.052	2.7	0.363	2.9	0.051	1.1	288	±62	317.8	±3.3	316.4	±6.6
BW28-16	7.60	93.00	178.00	0.54	0.051	8.4	0.348	8.5	0.050	1.2	239	±190	312	±3.6	291	±19
BW28-17	8.31	111.00	191.00	0.60	0.051	4.0	0.356	4.3	0.050	1.5	248	±92	317.5	±4.7	310	±10
BW28-18	14.90	229.00	345.00	0.68	0.054	2.0	0.374	2.2	0.050	0.9	371	±44	316.1	±2.9	320.8	±5.5
BW28-19	19.10	474.00	431.00	1.14	0.053	3.6	0.373	3.7	0.051	0.9	314	±81	322.8	±2.9	319	±5.8
BW28-20	15.30	365.00	358.00	1.05	0.053	2.1	0.366	2.3	0.050	0.9	344	±49	313.1	±2.9	308.7	±4.8
Spot	Element content, ppm			$^{232}Th/^{238}U$	Isotope ratio						Age and error					
	Pb	Th	U		$^{207}Pb/^{206}Pb$	±%	$^{207}Pb/^{235}U$	±%	$^{206}Pb/^{238}U$	±%	$^{207}Pb/^{206}Pb$	σ	$^{206}Pb/^{238}U$	σ	$^{207}Pb/^{235}U$	σ
G54-8 LA-ICP-MS zircon U-Pb																
G54-8-1	10.00	63.93	103.29	1.62	0.055	0.0	0.412	0.1	0.056	0.0	501.09	1.7	349.42	16.5	325.41	68.7
G54-8-4	8.49	55.34	73.31	1.32	0.064	0.0	0.408	0.1	0.050	0.0	466.56	517.8	314.26	22.9	320.31	72.8
G54-8-5	13.59	88.66	97.98	1.11	0.050	0.0	0.395	0.1	0.054	0.0	515.34	78.9	339.40	19.1	316.35	65.1
G54-8-6	14.12	99.74	129.93	1.30	0.057	0.0	0.401	0.1	0.052	0.0	533.80	277.2	324.45	16.6	320.01	66.0
G54-8-8	7.25	45.13	65.63	1.45	0.067	0.0	0.450	0.1	0.051	0.0	487.50	893.5	320.20	22.1	338.60	86.9
G54-8-9	14.35	91.68	113.02	1.23	0.061	0.0	0.412	0.1	0.052	0.0	548.97	242.7	329.02	17.8	328.71	64.9
G54-8-10	15.30	105.05	123.30	1.17	0.053	0.0	0.375	0.1	0.050	0.0	626.87	−394.6	314.22	17.0	306.24	56.9
G54-8-11	8.34	51.54	89.25	1.73	0.059	0.0	0.418	0.1	0.050	0.0	391.56	597.1	311.64	17.2	328.49	71.6
G54-8-13	8.84	55.45	100.79	1.82	0.058	0.0	0.390	0.1	0.049	0.0	488.58	135.3	309.16	18.3	319.72	54.3
G54-8-14	4.68	24.60	47.23	1.92	0.053	0.0	0.380	0.1	0.053	0.0	431.13	907.7	330.69	28.6	315.85	82.0
G54-8-19	12.07	75.33	107.69	1.43	0.050	0.0	0.373	0.1	0.053	0.0	493.01	−3.2	329.92	16.2	308.54	51.1
G54-8-21	8.53	59.68	97.45	1.63	0.054	0.0	0.389	0.1	0.049	0.0	535.79	23.1	309.72	19.2	316.42	57.7
G54-8-25	9.70	67.47	102.26	1.52	0.062	0.0	0.389	0.1	0.046	0.0	546.43	203.3	289.44	15.4	316.98	57.7
G54-8-26	18.28	126.25	139.75	1.11	0.051	0.0	0.379	0.1	0.054	0.0	458.63	−222.4	337.43	17.4	316.38	44.7
G54-8-28	21.32	153.53	170.22	1.11	0.054	0.0	0.374	0.1	0.051	0.0	345.85	264.3	319.25	13.7	310.69	49.1
G54-8-30	21.20	141.75	160.50	1.13	0.055	0.0	0.347	0.0	0.048	0.0	615.13	−255.7	303.75	14.5	304.62	41.3
G54-8-31	25.88	173.27	189.91	1.10	0.060	0.0	0.421	0.1	0.051	0.0	431.08	249.9	323.60	11.6	345.40	46.5
G54-8-32	6.56	41.80	75.61	1.81	0.056	0.0	0.384	0.1	0.052	0.0	498.05	106.9	328.88	21.4	312.51	58.2
G54-8-33	7.71	53.03	88.74	1.67	0.057	0.0	0.401	0.1	0.049	0.0	408.27	443.3	305.24	14.2	325.53	57.7
G54-8-34	23.57	154.45	172.19	1.11	0.055	0.0	0.413	0.1	0.055	0.0	311.26	323.0	347.09	12.8	339.36	48.6
G54-8-38	15.07	110.82	133.35	1.20	0.058	0.0	0.378	0.1	0.049	0.0	542.87	101.4	311.23	12.3	312.39	50.7
G54-8-39	11.97	84.14	122.79	1.46	0.053	0.0	0.344	0.1	0.050	0.0	569.14	−105.2	312.49	15.0	288.66	47.6
G54-8-40	8.60	54.97	99.37	1.81	0.056	0.0	0.388	0.1	0.051	0.0	530.13	196.5	320.47	19.0	316.78	56.4
G54-8-45	23.60	153.99	185.16	1.20	0.061	0.0	0.415	0.1	0.052	0.0	315.01	491.7	325.74	10.2	344.60	40.5
G54-8-47	9.22	57.91	88.13	1.52	0.057	0.0	0.382	0.1	0.052	0.0	632.30	−106.9	325.71	15.5	312.79	56.3
G54-8-50	122.79	908.60	351.74	0.39	0.057	0.0	0.381	0.0	0.049	0.0	189.25	481.1	306.71	8.7	323.59	29.2
G54-8-51	23.73	162.53	155.35	0.96	0.061	0.0	0.403	0.1	0.048	0.0	342.90	351.7	303.86	11.8	334.02	44.5
G54-8-54	20.22	123.47	147.01	1.19	0.055	0.0	0.416	0.1	0.056	0.0	337.12	268.7	348.10	13.2	355.74	41.8
G54-8-56	13.66	85.66	108.50	1.27	0.057	0.0	0.417	0.1	0.054	0.0	497.66	−2.4	339.35	11.5	341.92	48.9

G54-8-57	14.64	101.15	135.19	1.34	0.059	0.0	0.400	0.1	0.052	0.0	560.36	−66.9	324.21	16.3	329.59	48.7
G54-8-58	25.19	159.60	140.49	0.88	0.060	0.0	0.425	0.1	0.052	0.0	364.62	380.6	327.83	13.3	348.52	48.0
G54-8-62	14.55	95.26	136.12	1.43	0.054	0.0	0.402	0.1	0.054	0.0	527.63	130.7	340.09	15.7	330.06	51.1
G54-8-63	13.45	84.52	105.56	1.25	0.058	0.0	0.413	0.1	0.053	0.0	381.85	343.9	332.05	15.7	338.94	48.9
G54-8-65	194.18	1295.70	627.89	0.48	0.052	0.0	0.372	0.0	0.052	0.0	177.94	222.0	326.40	8.4	318.71	20.2
G54-8-67	16.17	103.82	115.38	1.11	0.053	0.0	0.362	0.1	0.049	0.0	546.88	50.3	308.39	16.4	300.98	49.7
G54-8-68	24.62	176.90	181.99	1.03	0.055	0.0	0.356	0.1	0.047	0.0	348.40	131.0	298.87	9.8	301.61	38.7
G54-8-70	20.55	144.99	179.58	1.24	0.050	0.0	0.341	0.1	0.049	0.0	443.51	−146.9	309.18	12.6	289.70	39.5
G54-8-71	10.29	71.60	110.82	1.55	0.049	0.0	0.331	0.1	0.048	0.0	555.69	−210.5	305.54	14.7	276.28	52.9
G54-8-72	20.85	141.74	167.39	1.18	0.057	0.0	0.384	0.1	0.049	0.0	295.26	393.1	305.90	12.6	322.40	39.3
G54-8-74	9.19	58.49	82.68	1.41	0.056	0.0	0.385	0.1	0.051	0.0	581.66	−29.8	318.13	16.2	313.68	58.3
G54-8-75	17.41	114.60	131.44	1.15	0.059	0.0	0.405	0.1	0.049	0.0	324.17	300.2	307.82	13.3	336.46	41.7
G54-8-79	14.35	89.92	123.90	1.38	0.060	0.0	0.403	0.1	0.048	0.0	521.95	102.2	300.21	14.5	326.18	57.6
G54-8-82	13.16	86.98	105.37	1.21	0.054	0.0	0.374	0.1	0.051	0.0	625.39	−62.5	319.54	16.5	306.57	56.5
G54-8-85	23.60	159.07	172.07	1.08	0.049	0.0	0.350	0.0	0.052	0.0	353.95	62.2	327.67	13.6	307.18	42.6
G54-8-86	11.37	86.85	87.01	1.00	0.053	0.0	0.364	0.1	0.050	0.0	513.27	−180.5	315.02	20.7	302.92	48.7
G54-8-90	3.70	29.31	45.32	1.55	0.064	0.0	0.459	0.1	0.053	0.0	456.23	685.5	330.49	19.9	353.03	78.4
G54-8-92	44.81	285.46	195.08	0.68	0.056	0.0	0.422	0.1	0.054	0.0	335.13	242.7	338.32	13.9	347.34	45.2
G54-8-94	13.83	89.38	108.71	1.22	0.060	0.0	0.407	0.1	0.050	0.0	551.81	284.6	311.63	14.7	334.10	50.0
G54-8-98	5.55	33.25	58.29	1.75	0.064	0.0	0.415	0.1	0.050	0.0	510.44	598.0	312.78	20.9	328.46	69.1
G54-8-99	10.01	59.90	106.51	1.78	0.050	0.0	0.383	0.1	0.054	0.0	437.80	151.0	337.47	11.6	315.54	51.6
G54-8-100	54.60	343.55	213.82	0.62	0.059	0.0	0.450	0.1	0.055	0.0	315.13	329.4	344.39	9.7	371.29	35.3

lithophile element enrichment (especially Pb enrichment) are typical characteristics of magma in subduction zones, indicating that their source region was strongly influenced by the dehydration fluids released from subducting slabs. In contrast, the volcanic rocks in Eastern Junggar and West Tianshan lack Nb-Ta depletion (Nb/La $\approx$1), suggesting that they may have formed in an intra-plate extensional setting (such as a rift or post-collision spreading) where the magma source region was less affected by subduction fluids.

The Zr/Nb (29.36–65.60) and Hf/Ta (12. to 30.16) ratios of the samples are significantly higher than those of Ocean island basalt (OIB: Zr/Nb = 5.8, Hf/Ta = 2.9) or normal mid-ocean ridge basalt (N-MORB: Zr/Nb = 30, Hf/Ta = 2.9). The volcanic samples exhibit low initial $(^{87}\mathrm{Sr}/^{86}\mathrm{Sr})_i$ values (0.703941–0.705675) and positive $\varepsilon_{\mathrm{Nd}}(t)$ values (7.5–8.0), indicating that their source was predominately a relatively depleted mantle with minor contamination from subducted sediments. In contrast, the volcanic rocks from Eastern Junggar, with low $\varepsilon_{\mathrm{Nd}}(t)$ (4.0–6.0) and low Sr isotopes (0.7030–0.7040), reflect a more depleted mantle source (likely linked to asthenospheric upwelling), whereas the rocks from Western Tianshan, characterized by low $\varepsilon_{\mathrm{Nd}}(t)$ (−2.0 to +1.0) and high Sr isotopes (0.7060–0.7080), suggest significant contamination by ancient crustal materials, consistent with an intracontinental rift or post-collisional extensional setting (Pan et al., 2022). In the Sr-Nd isotope diagram (Fig. 6(a)), the samples plot close to the early Carboniferous island arc volcanic rocks from Western Junggar, implying a magmatic source similar to the Junggar oceanic crust. Compared to Hatu back-arc basalt, Baikouquan volcanic rocks have higher $\varepsilon_{\mathrm{Nd}}(t)$ values, suggesting derivation from a more depleted mantle source (Xiao et al., 2023). This is corroborated by the $(^{87}\mathrm{Sr}/^{86}\mathrm{Sr})_i$–$(^{143}\mathrm{Nd}/^{144}\mathrm{Nd})_i$, $(^{206}\mathrm{Pb}/^{204}\mathrm{Pb})_i$–$(^{207}\mathrm{Pb}/^{204}\mathrm{Pb})_i$, and $(^{206}\mathrm{Pb}/^{204}\mathrm{Pb})_i$–$(^{208}\mathrm{Pb}/^{204}\mathrm{Pb})_i$ diagrams (Fig. 6(c), (d), (e), (f)), in which the datapoints fall near the mantle evolution line, indicating a depleted MORB-like mantle component in the source. As immobile elements, Zr and Nb are effective tracers of magmatic source properties. In the Zr-Nb diagram (Fig. 8(a)), the samples display characteristics of a depleted mantle. Th and Ta are highly incompatible elements closely associated with subduction, maintaining nearly constant ratios during mantle melting (Xiao et al., 2023). However, during plate subduction, Th is more mobile than Ta, leading to their fractionation and resulting in high Th/Yb ratios in subduction-zone volcanic lavas (Xiao et al., 2023). Additionally, minor sediment melts can elevate the Th content, causing positive anomalies (Plank, 1988; Hawkesworth et al., 1997). The Th/Yb ratio thus reflects the contribution of sediment melts to the source magma (Elliott et al., 1997; Class et al., 2000; Singer et al., 2007). In the Th/Zr-U/Th diagram (Fig. 8(b)), the samples exhibit a vertical trend, suggesting the involvement of subduction-derived fluids. The Ce/Pb values (2.52–13.38, average 4.61) are significantly lower than those of depleted mantle source magma (Hofmann, 1988), further depleted by subduction-zone fluids (Klein and Karsten, 1995). Collectively, these observations, combined with the Th/Zr-U/Th diagram, indicate that the Kebai Fault Zone volcanic rocks experienced metasomatism by subduction fluids during their formation. The relatively concentrated Th/Yb and Ta/Yb values, with the Th/Yb values higher than the MORB values, suggest that mantle magma was metasomatized by subduction fluid and melts. The melting of subduction-related sediments introduced Th into the mantle wedge, increasing its concentration and causing deviations from the mid-ocean ridge mantle evolution trend, including the elevated Th/Yb ratios characteristic of subduction-modified sources.

The content and ratios of earth elements and high-field strength elements are often used to identify magma source

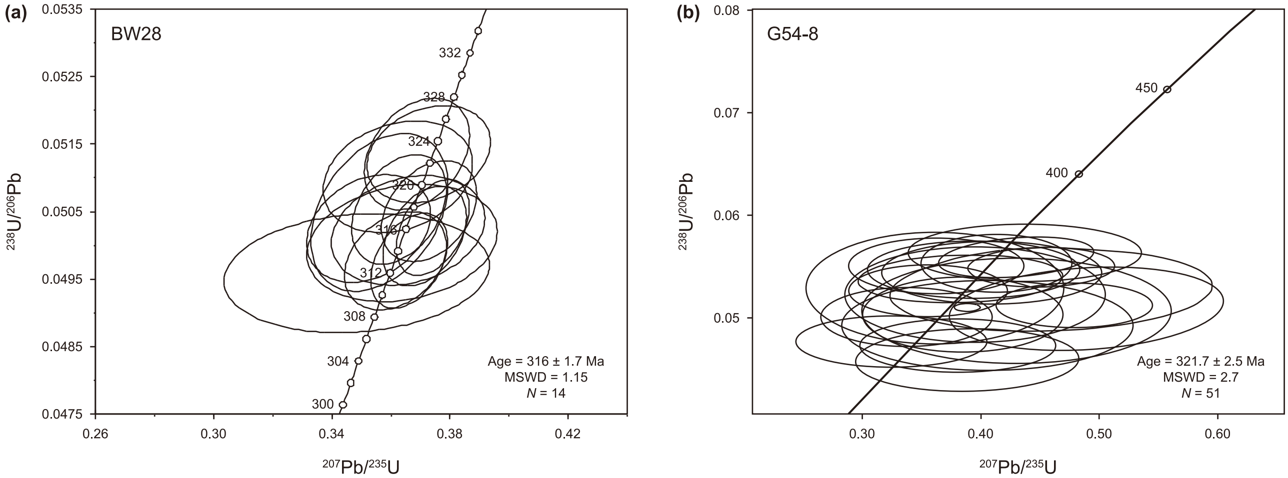

Fig. 5. U-Pb isotopic age of zircon from Late Carboniferous volcanic rocks in Kebai Fault Zone.

Table 3
Sr-Nd-Pb isotopic composition of Late Carboniferous volcanic rocks in Kebai Fault Zone.

Sample		G53-3	G53-4	G54-8	G54-10	G53-12	B55-3
Isotopic initial ratio correction age, Ma		316	316	316	316	316	316
Sr isotopes	Rb, ppm	11.6	12.6	2.03	9.51	18	1.41
	Sr, ppm	515	491	161	1381	433	204
	$^{87}Sr/^{86}Sr$	0.703926775	0.703935623	0.704046657	0.704351879	0.705564957	0.705670542
	$(^{87}Sr/^{86}Sr)_i$	0.703941	0.703952	0.704055	0.704356	0.705592	0.705675
	2σ	0.000006	0.000007	0.000008	0.000005	0.000009	0.000007
Nd isotopes	Sm, ppm	2.10	2.00	1.90	1.80	3.70	7.80
	Nd, ppm	7.10	6.70	7.30	6.40	13.00	29.00
	$^{147}Sm/^{144}Nd$	0.17872	0.18037	0.15727	0.16995	0.17198	0.16252
	$(^{143}Nd/^{144}Nd)_i$	0.512232	0.512232	0.512232	0.512232	0.512232	0.512232
	2σ	0.000011	0.000009	0.000007	0.000010	0.000011	0.000011
	$\varepsilon_{Nd}(t)$	7.5	7.5	8.0	7.5	8.0	8.0
	T_{DM}, Ma	728	741	508	652	573	527
	T_{2DM}, Ma	466	464	429	469	428	429
Pb isotopes	Pb, ppm	3.34	3.06	2.86	2.09	4.42	6.07
	Th, ppm	0.71	0.7	0.89	0.57	2.03	0.74
	U, ppm	0.23	0.25	0.3	0.21	0.64	0.28
	$^{208}Pb/^{204}Pb$	37.9970	38.0150	38.0840	38.0400	38.1960	37.8520
	$^{207}Pb/^{204}Pb$	15.5150	15.5170	15.5150	15.5140	15.5270	15.5010
	$^{206}Pb/^{204}Pb$	18.1390	18.1450	18.2300	18.2110	18.3400	18.0670
	$(^{208}Pb/^{204}Pb)_i$	37.7834	37.7851	37.7712	37.7659	37.7344	37.7295
	$(^{207}Pb/^{204}Pb)_i$	15.5037	15.5036	15.4978	15.4976	15.5033	15.4935
	$(^{206}Pb/^{204}Pb)_i$	17.9254	17.8916	17.9047	17.8994	17.8910	17.9239

regions and melting degree (Aldanmaz et al., 2000). With an increase in the degree of partial melting, the Sm content gradually decreases relative to that of the heavy rare earth elements (Aldanmaz et al., 2000). Partial melting of spinel peridotite does not significantly change the Sm/Yb and La/Sm values, whereas partial melting of garnet dipyroxene peridotite significantly changes the Sm/Yb values. The Sm/Yb-Sm diagram (Fig. 8(c)) shows that the volcanic rocks in the Kebai Fault Zone fall on the evolution curve of garnet spinel dipyroxene peridotite, indicating that the source area was mainly garnet and spinel dipyroxene peridotite, and that 10%–30% melting occurred, which is similar to the melting degree of the Baikouquan volcanic rocks and the porphyry basalt of the Hala'alat Formation (20%–30%) (Xiang et al., 2015; Xiao et al., 2023). In the Ta/YB-TH/Yb diagram (Fig. 8(d)), the samples fell into the inter-oceanic arc region, similar to the basaltic andesite in the Baikouquan area (Xiao et al., 2023).

Therefore, the unique geochemical features of the Carboniferous volcanic rocks in the Kebai Fault Zone (Nb-Ta depletion, large ion lithophile element enrichment, and calcalkaline series) show significant differences from those in surrounding areas. These differences consistently point to their formation in a post-arc basin extensional environment, related to island arc magmatism. The source area might be the mantle wedge, modified by subduction sediment melts and fluids and having undergone partial melting. In addition, there is evidence of a small amount of crustal contamination. In contrast, the volcanic rocks in other regions (such as the bimodal volcanism in Eastern Junggar and the alkaline series in Western Tianshan) are more closely related to intra-plate

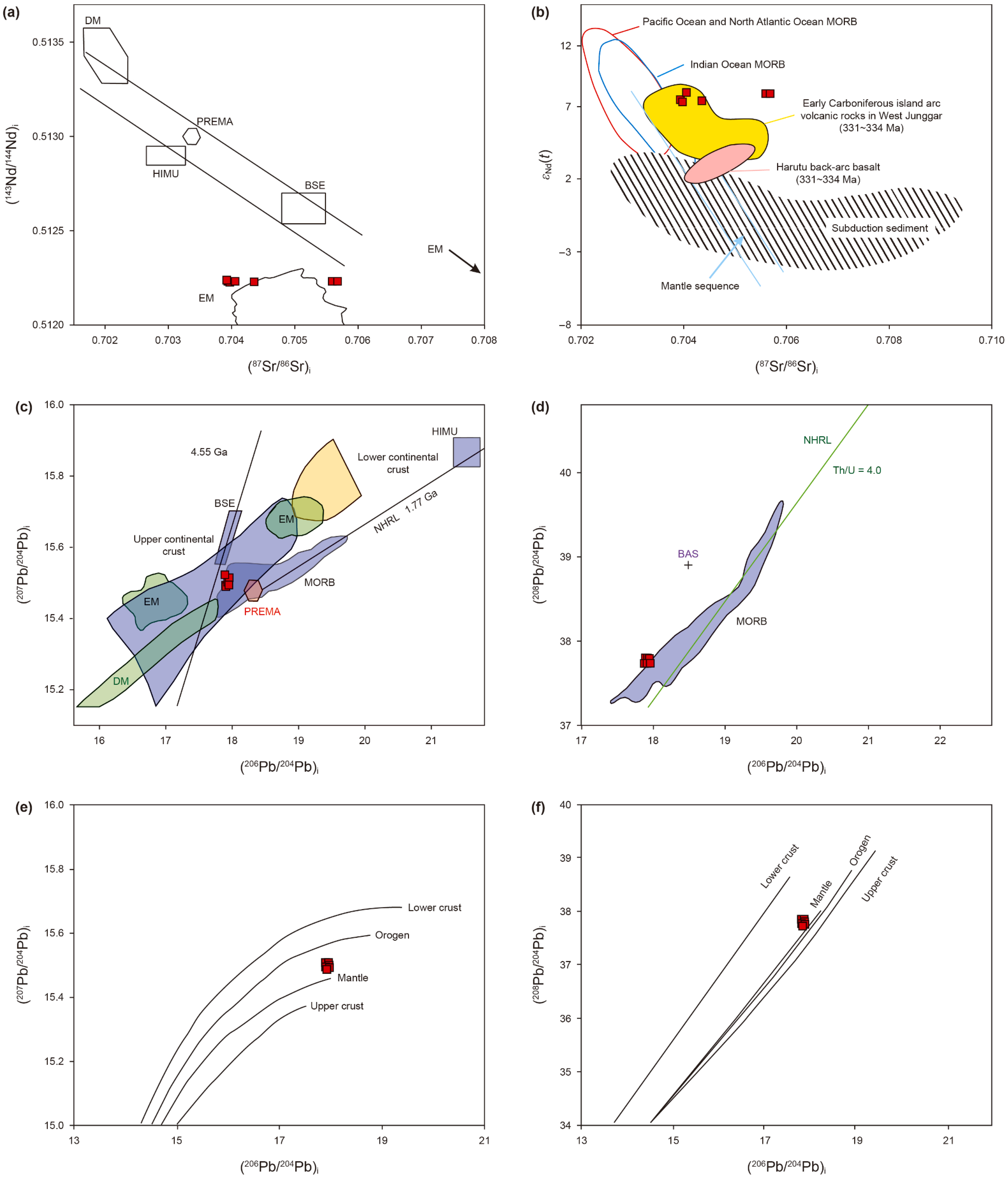

Fig. 6. Sr, Nd, Pb isotopic diagrams of Late Carboniferous volcanic rocks in Kebai Fault Zone. **(a)** ^{143}Nd/^{144}Nd vs. ^{87}Sr/^{86}Sr isotope discrimination diagram (according to Xiao et al. (2023); **(b)** ε_{Nd} vs. (^{87}Sr/^{86}Sr) isotope discrimination diagram (according to Zindler and Hart (1986)); **(c)** and **(e)** ^{207}Pb/^{204}Pb vs. ^{206}Pb/^{204}Pb lead isotope discrimination diagram (according to Allègre (1988)); **(d)** and **(f)** ^{208}Pb/^{204}Pb vs. ^{206}Pb/^{204}Pb lead isotope evolution curve discrimination diagram for crust and mantle (according to Zartman (1981)).

extension or crustal contamination mechanisms. This reveals the diversity of magmatic responses in different tectonic units during the closure of the Paleo-Asian Ocean. In the future, it will be necessary to include deep geophysical data (such as mantle structure) to further verify the dynamic relationship between the morphology of the subducted plate and magmatic activity.

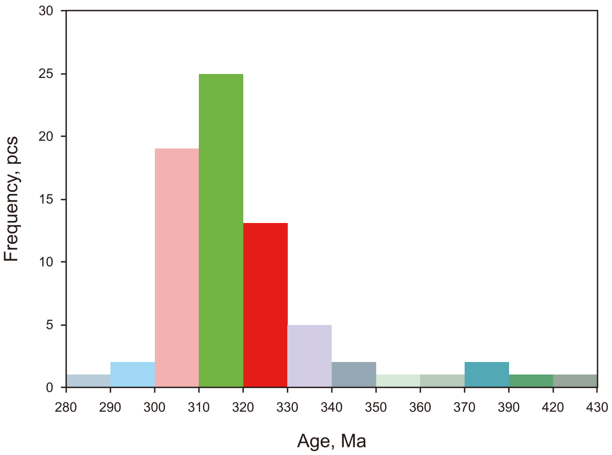

Fig. 7. Age histogram of volcanic rocks in Western Junggar and its vicinity.

5.3. Tectonic environment and significance

The Late Carboniferous andesite in Western Junggar has the typical characteristics of a subduction zone arc volcanic rock, originating from the partial melting of a water-rich mantle wedge, related to the dehydration of the subducting slab. The zircon U-Pb age (about 322 Ma) indicates that, in the mid-Carboniferous, the residual oceanic basin was still subducting and not completely closed, creating an arc-back extensional environment. Han et al. (2006) believes that subduction consumption in the southern part of Western Junggar ended during the Late Carboniferous–early Permian, and that the region was a post-collision extensional environment. The volcanic rocks exposed in the Baobei and Bagutu areas have formation ages of 358–332 Ma, formed in an Early Carboniferous island arc environment (Wang et al., 2007; Guo et al., 2010), while the Bagutu–Darbut area is an intra-oceanic island arc environment (Shen et al., 2013), and the basic-neutral volcanic rocks in the Hatu–Bagutu area have formation ages of 325–324 Ma, belonging to an arc-back basin. The andesite north of Urho has a formation age of 306–304 Ma and was still formed in an island arc environment (Li et al., 2016). Liu et al. (2009) identified E-MORB-type basalt in Darbut, suggesting that subduction may have continued until the Late Carboniferous (302 Ma). Xiao et al. (2023) believes that the volcanic rocks in the Baikouquan area are related to the subduction consumption of the late Paleozoic oceanic basin in Western Junggar. During the Carboniferous period in Western Junggar, the subduction and reduction of the oceanic basin caused intense island arc magmatism, which was an important magmatic event in the inner arc of the Junggar Ocean. Li et al. (2016) proposed that a set of basic volcanic rocks in the Urho area showed “lagged arc” characteristics in the early Permian (~283 Ma), and believe that subduction in Western Junggar ended in the late to early Permian. The early Carboniferous adakitic rock walls (334 Ma) in the northern part of Western Junggar are related to low-angle slab subduction, while the Late Carboniferous rock walls in the southern part may be affected by mid-ocean ridge subduction. Overall, this demonstrates the multi-stage subduction-closure process of the ancient Asian Ocean (Yin et al., 2012). Xiao et al. (2023) obtained a zircon U-Pb age of 342 Ma for basaltic andesite from the Baikouquan area, indicating that there was magmatism in Western Junggar in the early Carboniferous, consistent with the island arc environment era. The petrogenesis of these rocks was related to slab subduction and the source area was affected by subducted sediments, all indicating that this volcanic rock is likely related to the subduction consumption of the late Paleozoic oceanic basin in Western Junggar. Tang et al. (2010) studied the exposed basalt in the Hatu area and obtained a crystallization age of 315–290 Ma (early to Late Carboniferous. These rocks are mid-ocean ridge basalt (MORB)-like tholeiites, indicating they are products of a mid-ocean ridge subduction system. In Western Tianshan, Carboniferous alkaline bimodal volcanic rocks (basalt–rhyolite association) developed, which may indicate an intra-continental rift environment related to post-plate suture extension (Li et al., 2006). In the eastern part of the Junggar Basin, there is a regional unconformity at the top of the Carboniferous strata, which may reflect a tectonic event involving the transition from compression to extension, rather than post-arc extension (Yi et al., 2018). The Early Carboniferous adakitic rock walls in northern Xinjiang may reflect different tectonic mechanisms (such as delamination or underplating) rather than a unified post-arc system. They may originate from the partial melting of the lower crust due to delamination, rather than the melting of the subducted slab (Yin et al., 2015). In the Late Carboniferous, the Junggar Basin transitioned from marine to terrestrial sedimentation, which may be accompanied by gravitational collapse after crustal thickening, triggering an extensional environment (Yi et al., 2018). However, the trace element characteristics of the andesite (such as Nb-Ta deficiency and Pb enrichment) are consistent with the melting of the mantle wedge by subduction zone fluids, which is difficult to explain using rift or delamination mechanisms (Yin et al., 2015; Shao et al., 2022). Although the high Sr/Y ratio and low Yb content of adakite may originate from various mechanisms, their spatiotemporal distribution is highly consistent with melting conditions against a background of low-angle subduction (Yin et al., 2015). The residual oceanic basin in Western Junggar was not completely closed in the Middle Carboniferous (about 322 Ma), and subduction continued until the Late Carboniferous, connecting with the back-arc extension stage after the closure of the Darbut–Kalamaili Oceanic Basin (Chen and Arakawa, 2005; Shao et al., 2022). The difference between the low-angle subduction in the north and mid-ocean ridge subduction in the south can explain the diversity of rock assemblages in different regions, while overall, they still represent segmented responses of the subduction system (Chen and Arakawa, 2005; Yin et al., 2015). A trench-arc-basin system (forearc-island arc-backarc) was explicitly developed in Western Tianshan during the Early Carboniferous, while in the Late Carboniferous, the tectonic sequence in the eastern part of the Junggar Basin showed intra-continental extension, which may have been a continuation of the transformation from back-arc basin to continent (Chen and Arakawa, 2005; Yi et al., 2018). Based on multi-dimensional evidence, including petrological geochemistry, chronology, and regional tectonic evolution, a back-arc basin tectonic environment can explain the spatiotemporal differentiation characteristics of the Late Carboniferous magmatic activity in Western Junggar. Other tectonic explanations (such as rift or delamination environments) can explain local phenomena, but lack a systematic connection to the regional subduction background. Further research is needed to combine deep geophysical data (such as mantle structure) and high-precision chronological frameworks to clarify the dynamic relationships between subduction plate morphology and magmatic responses.

Table 4
Statistical table of age results of volcanic rocks in Western Junggar and its vicinity.

Location or sampling well	Lithology	Zircon U-Pb for age, Ma	Test method	Sources of date
SiCan 1	Tuff	354.6 ± 2.6	LA-ICP-MS	Li et al. (2016)
HongShan 4	Tuff	318.3 ± 5.1	LA-ICP-MS	
	Tuff	322.0 ± 23	LA-ICP-MS	
Guai 26	Granite	327.3 ± 33	SIMS	
JinLong 5	Granite	324.6 ± 2.1	SIMS	
Guai 3	Basalt	303.1 ± 3.4	SIMS	
Jin 9	Tuff	313.5 ± 53	LA-ICP-MS	
	Tuff	325.1 ± 2.4	LA-ICP-MS	
	Tuff	335.8 ± 2.7	LA-ICP-MS	
Ke 85	Tuffite	289.5 ± 12	LA-ICP-MS	
	Tuffite	331.3 ± 2.6	LA-ICP-MS	
XiaJi 2	Tuff	323.5 ± 1.8	LA-ICP-MS	
XiaGu 2	Tuffite	312.9 ± 1.2	LA-KP-MS	
MoShen 1	Tuffite	331.7 ± 3.8	SHRIMP	
ShiXi 4	Dacite	297.3 ± 4.4	LA-ICP-MS	
	Rhyolite	307.2 ± 7.9	LA-ICP-MS	
MaDong 4	Dacite	326.6 ± 2.8	SIMS	
DiXi 14	Tuff	337.2 ± 4.1	SHRIMP	
LuDong 1	Tuff	313.3 ± 4.6	LA-ICP-MS	
ShiNan 1	Basalt	306.8 ± 4.7	SIMS	
DiZhong 1	Tuff sandstone	314.6 ± 1.2	LA-ICP-MS	
Ying 2	Tuff	319 ± 11	LA-ICP-MS	
SanCan 1	Basalt	300.4 ± 1.3	SIMS	Su et al. (2010)
WuCan 1	Tuff	324.3 ± 2.3	LA-ICP-MS	Li et al. (2016)
LunCan 1	Tuffite	397.9 ± 1.7	LA-ICP-MS	
Lun 8	Dacite	376.6 ± 4.1	SIMS	
Lun 5	Andesite	313.4 ± 53	SIMS	
GuCheng 1	Tuff	317.7 ± 3.1	LA-ICP-MS	
DongQuan 1	Andesite	316.1 ± 2.7	LA-ICP-MS	
Cai 58	Tuff	325.0 ± 4.7	LA-ICP-MS	
JiCan 1	Basalt	313.2 ± 2.1	SIMS	
FuQian 1	Dacite	315.4 ± 16	LA-ICP-MS	
	Basaltic andesite	317.4 ± 2.1	LA-ICP-MS	
TaCan 1	Tuff	315.3 ± 1.6	LA-ICP-MS	
ZhaoCan 1	Diorite	421.9 ± 3.1	SIMS	
North of Baijiantan	Dacitic tuff	345.1 ± 2.0	Zircon U-Pb	Xinjiang Oilfield (2022)
	Andesite	374.6 ± 3.6	LA-ICP-MS	
424	Basaltic andesite	306.2 ± 5.8	LA-ICP-MS	
Bai 72	Rhyolite	303.2 ± 4.8	LA-ICP-MS	
	Granite	300 ± 3.6	LA-ICP-MS	
	Concomitant conglomerate basalt	302.4 ± 5.0	LA-ICP-MS	
Gu 96	Amygdaloidal andesite	314.1	LA-ICP-MS	
Gu 131	Amygdaloidal andesite	314	LA-ICP-MS	
Ke 84	Amygdaloidal basalt	307.1	LA-ICP-MS	
555	Glauconite-bearing fine-grained debris sandstone	306	LA-ICP-MS	
Gu 66	Basaltic andesite	303 ± 2	LA-ICP-MS	
	Basalt	304 ± 3	LA-ICP-MS	
Feng 19	Andesite	295	LA-ICP-MS	
CheTan 1	Andesite	310.7 ± 2.9	LA-ICP-MS	
	Andesite	312.9 ± 3.2	LA-ICP-MS	
Urho	Rich porphyry basalt	302 ± 2	LA-ICP-MS	Li et al. (2024)
Baikouquan	Basaltic andesite	342.2 ± 1.0	LA-ICP-MS	Xiao et al. (2023)
Urhe section	Grayish green basaltic andesite	304 ± 3.5	LA-ICP-MS	Tong (2023)
	Light grey-green lithic tuff	304 ± 4.3	LA-ICP-MS	
	Purple andesite	308.5 ± 3.9	LA-ICP-MS	
	Yellowish brown rhyolite	308.9 ± 2.3	LA-ICP-MS	
	Grey-purple basalt porphyrite	305.9 ± 2.0	LA-ICP-MS	
	Bronzing amygdaloidal basalt	303.3 ± 3.7	LA-ICP-MS	
BW28	Rhyolitic crystal tuff	316.8 ± 1.7	SHRIMP	This study
G54	Basalt	321.7 ± 1.8	LA-ICP-MS	
B527	Rhyolitic crystal tuff	316.3 ± 2.9	SHRIMP	Xinjiang Oilfield (2025)
430	Rhyolitic crystal tuff	316.2 ± 2.2	SHRIMP	
440	Rhyolitic crystal tuff	315.2 ± 2.7	SHRIMP	

Owing to the varying sensitivities of different element suites to magma source properties, degrees of partial melting, and evolutionary processes, there are distinct differences in the geochemical information captured by Hf-Th-Ta and Zr-Nb-Y assemblages. Ratios of high field strength elements to incompatible elements, such as those in the Hf/3-Th-Ta diagram (Fig. 9(a)), are used to characterize tectonic environments. Volcanic samples from the Kebai Fault Zone plot within the calc-alkaline basalt field of the island arc, indicating a tectonic setting associated with the subduction of the Junggar Ocean. Specific element behaviors allow further classification of island arcs into intra- or marginal arcs (Xiao et al., 2023), as their migration and enrichment trends reflect ocean–continent transformation and evolutionary stages. In the Ta/YB-TH/Yb diagram (Fig. 8(d)), the Kebai Fault Zone volcanic rocks exhibit low

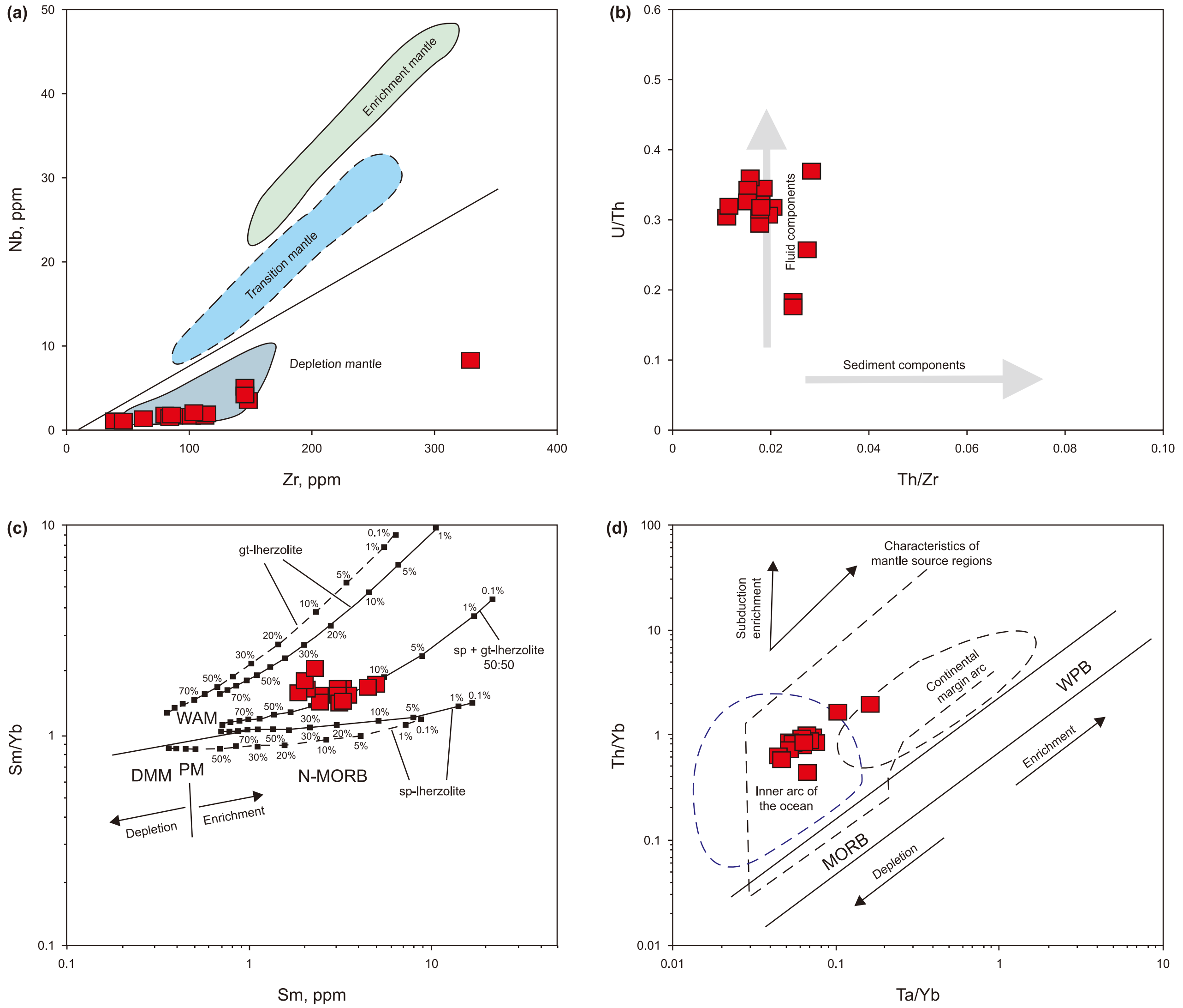

Fig. 8. Geochemical discrimination diagrams. **(a)** Nb vs. Zr diagram for mantle endmember (according to Pearce and Cann (1973)), **(b)** U/Th vs. Th/Zr diagram indicating marine organism and sediment component signatures (according to Pearce (1982)), **(c)** Sm/Yb vs. Sm diagram for mantle enrichment-depletion and rock type (WAM, N-MORB, etc.) discrimination (according to Hawkesworth et al. (1997)), **(d)** Th/Yb vs. Ta/Yb diagram for tectonic setting (MORB, island arc, WPB) and mantle source discrimination (according to Aldanmaz et al. (2000)).

Th/Yb (0.61–1.91) and Ta/Yb (0.04–0.16) ratios, with the data plotted within the inner arc field, comparable to the basaltic andesite from the Baikouquan area (Xiao et al., 2023).

The spider diagram of the normalized trace elements in the original mantle (Fig. 3(a) and (b)) shows that large ion lithophilic elements, such as Ba, Th, U, and Sr, are relatively enriched, whereas high field strength elements, such as Nb, Ta, Zr, and Hf, are relatively depleted, characteristics typical of island arc volcanic rocks associated with subduction. This suggests that the tectonic environment was closely related to an island arc. Previous studies have shown that the Late Carboniferous to Early Permian was an ocean–continental transition period in the southern part of Western Junggar, that the region comprised mainly island arc environments related to subduction (Zhang et al., 2006; Yin et al., 2012; Xiang et al., 2015; Li et al., 2016) and post-collision extension (Han et al., 2006; Zheng et al., 2007), and arguing that Western Junggar was formed in an inter-oceanic arc environment (Chen et al., 2005; Zheng et al., 2007; Zhang et al., 2011). Because of the uniqueness of elements such as Zr and Y to magma differentiation and the characteristics of the source area, in the Nb × 2-Zr/4-Y discriminant diagram (Fig. 9(b)), all samples fell within the range of intra-plate tholeiitic, N-MORB, and volcanic arc basalt. Using the content relationship between the large ion lithophilic element V and the transition metal element Ti, the sample points in the V-Ti/1000 discrimination diagram (Fig. 9(c)) fell in the overlapping areas of the mid-ocean ridge and back-arc basin basalt. In contrast, in the La/10-Y/15-Nb/8 discrimination diagram (Fig. 9(d)), the sample points fell in the overlapping areas of calc-alkaline and volcanic arc basalt. This reveals that the samples were composed of both mid-ocean ridge basalt and island arc igneous rocks. Therefore, the genesis of the volcanic rocks in the Kebai Fault Zone was controlled by ocean ridge extension and subduction, reflecting a tectonic environment of extension in a back-arc basin.

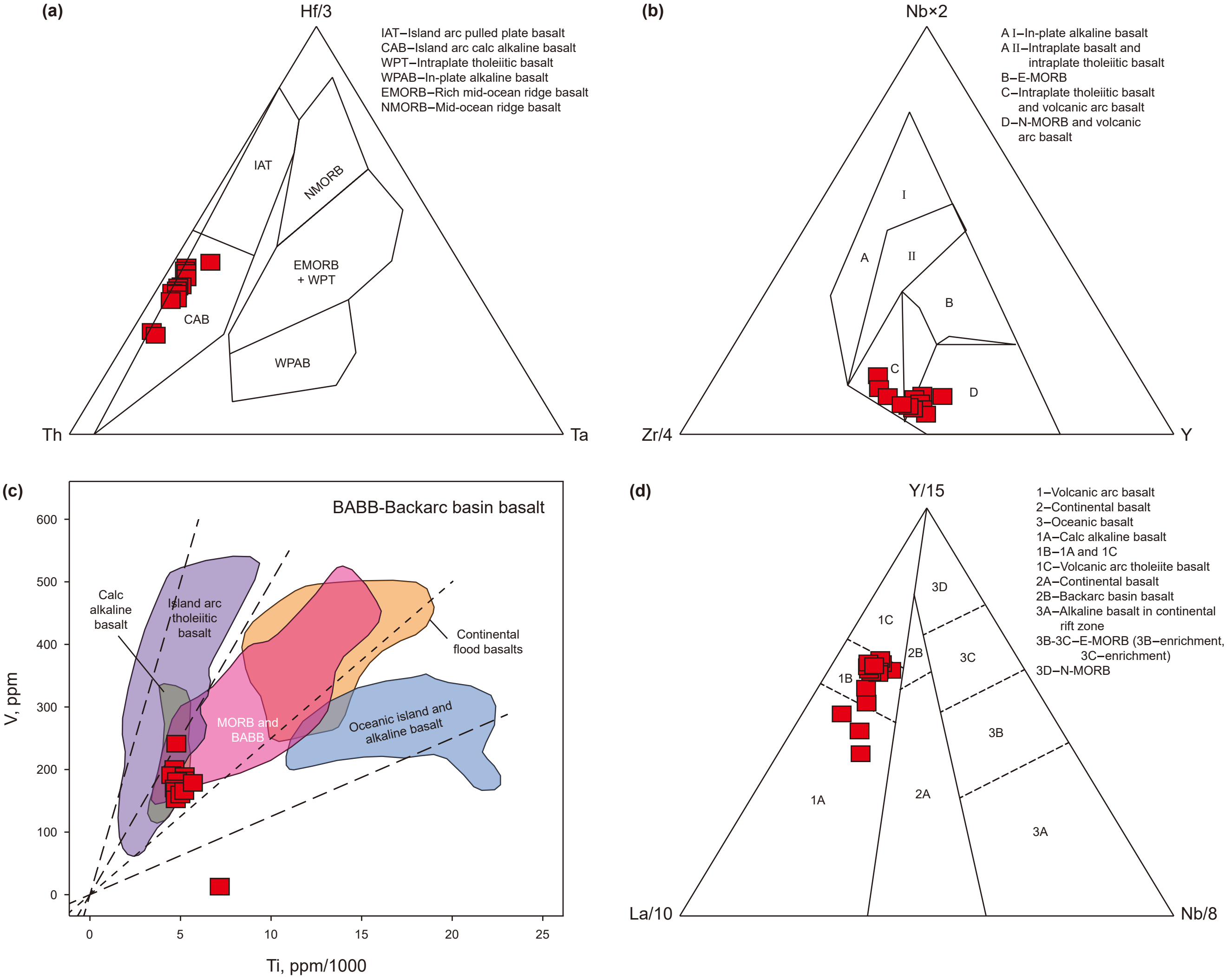

Fig. 9. (**a**) Th-Hf-Ta diagram of the Kebai Fault Zone (according to Wood (1980)), (**b**) Nb × 2-Zr/4-Y discrimination diagram (according to Meschede (1986)), (**c**) V-Ti/1000 discrimination diagram (according to Shervais (1982)) and (**d**) La/10-Y/15-Nb/8 discriminant chart (according to Cabanis and Lecolle (1989)).

6. Conclusions

(1) Zircon U-Pb chronology results showed that the SHRIMP U-Pb age of the tuff in the Kebai Fault Zone is 316.8 ± 1.7 Ma, and the LA-ICP-MS zircon U-Pb age of the andesite is 321.7 ± 1.8 Ma, representing a Late Carboniferous volcanic eruption age. The horizon can be compared with the upper Chengjisihanshan Formation in the region.

(2) The volcanic rocks in the Kebai Fault Zone are calc-alkaline rocks, and are sodium-rich and potassium-poor. The consolidation index (SI) ranged from 8.53 to 25.84, indicating a high degree of crystallization differentiation. Their light rare earth elements are relatively enriched, while their heavy rare earth elements are relatively depleted. The light and heavy rare earth elements are clearly differentiated. Large ion lithophile elements, such as Ba, Th, U, and Sr, are relatively enriched and high field strength elements, such as Nb, Ta, Zr, and Hf, are relatively depleted. The source area was primarily composed of garnet and spinel diopside peridotite and underwent 10%–30% melting.

(3) The Zr/Nb and Hf/Ta values are higher than those of ocean island basalts or standard mid-ocean ridge basalts, the $(^{87}Sr/^{86}Sr)_i$ values are lower, and the $\varepsilon_{Nd}(t)$ values are positive. The Sr-Nd-Pb isotopes showed affinities similar to those of the mantle, along with a small amount of crustal contamination. Combined with the Hf/3-Th-Ta, Nb × 2-Zr/4-Y, V-Ti/1000, and La/10-Y/15-Nb/8 tectonic environments, it is considered that the genesis of the volcanic rocks in the Kebai Fault Zone was controlled by the extension of the ocean ridge and subduction, with a tectonic environment of extension in a back-arc basin.

CRediT authorship contribution statement

Wei Wang: Writing – original draft, Methodology. **Chuan-Yi Tang:** Project administration. **Zong-Quan Yao:** Writing – review & editing, Funding acquisition, Conceptualization. **Yan Gao:** Supervision, Resources. **Feng-Bin Han:** Software. **Zong-Rui Xie:** Validation, Investigation. **Jian Chen:** Visualization. **Yuan-Feng Yang:** Supervision. **Ya-Fang Zhang:** Visualization.

Data availability

The data used to support the findings of this study are included in the article.

Declaration of interest statement

The authors declare that there are no conflicts of interest regarding the publication of this paper.

Acknowledgments

This research was supported by the Tianshan Talent Training Program (2023TSYCCX0002), Outstanding Graduate Innovation Project of Xinjiang University: "Genesis and Exploration Significance of Carboniferous Volcanic Rocks in the Kebai Fault Zone, West Junggar"(XJDX2025YJS108), Key Research and Development Plan of Xinjiang Autonomous Region "Establishment of Xinjiang Coalbed Methane Geological Evaluation Standards" project (2017B03019-1), and Baikouquan Oil Production Plant of Xinjiang Oilfield Company "Study on Sequence and Reservoir Characteristics of Carboniferous system in upper wall of Kebai Fault." The authors are grateful to Yong Wang from the Institute of Geomechanics at the Chinese Academy of Geological Sciences for his experimental guidance. They would also like to thank Professor Chuanlin Zhang from Hohai University and Researcher Ping Shen from the Institute of Geology and Geophysics, Chinese Academy of Sciences, for their helpful suggestions.

References

Aldanmaz, E., Pearce, J.A., Thirlwall, M.F., et al., 2000. Petrogenetic evolution of late Cenozoic, post-collision volcanism in Western Anatolia, Turkey. J. Volcanol. Geoth. Res. 102 (1–2), 67–95. https://doi.org/10.1016/S0377-0273(00)00182-7.

Allègre, C.J., Lewis, E., Dupré, B., 1988. A coherent crust-mantle model for the uranium-thorium-lead isotopic system. Chem. Geol. 70 (3), 211–234. https://doi.org/10.1016/0009-2541(88)90094-0.

Cabanis, B., Lecolle, M., 1989. Diagram La/10-Y/15-Nb/8: a tool for discriminating volcanic series and demonstrating mixing and/or crustal contamination processes. In: Proceedings of the Academy of Sciences, Serie II, 309, pp. 2023–2029 (in French).

Chen, B., Arakawa, Y., 2005. Elemental and Nd-Sr isotopic geochemistry of granitoids from the West Junggar foldbelt (NW China), with implications for Phanerozoic continental growth. Geochem. Cosmochim. Acta 69 (5), 1307–1320. https://doi.org/10.1016/j.gca.2004.09.019.

Chen, F.J., Wang, X.W., Wang, X.W., et al., 2005. Prototype and tectonic evolution of Junggar Basin. Earth Sci. Front. 12 (3), 77–89. https://doi.org/10.3321/j.issn:1005-2321.2005.03.010 (in Chinese).

Choulet, F., Faure, M., Cluzel, D., et al., 2012. From oblique accretion to transpression in the evolution of the Altaid collage: new insights from West Junggar, northwestern China. Gondwana Res 21 (2–3), 530–547. https://doi.org/10.1016/j.gr.2011.07.015.

Class, C., Miller, D.M., Goldstein, S.L., et al., 2000. Distinguishing melt and fluid subduction components in Umnak Volcanics. Aleutian Arc. G-cubed (1), 115355. https://doi.org/10.1029/1999GC000010.

Dobretsov, Q., Li, Y.J., et al., 1995. Petrogenesis and geodynamic setting of the late Carboniferous granodiorite porphyry in Miaoergou pluton, southern West Junggar. Acta Petrol. Sin. 37 (4), 1159–1176. https://doi.org/10.18654/1000-0569/2021.04.12 (in Chinese).

Dong, X.M., Zha, M., Jiang, Y.Q., et al., 2013. Reservoir characteristics, evolution and genetic model of Carboniferous volcanic rocks in northern Xinjiang. Journal of Xi'an Shiyou University (Natural Science Edition) 28 (4), 8–16. https://doi.org/10.3969/j.issn.1673-064X.2013.04.002 (in Chinese).

Duan, F.H., Zhi, Q., Li, Y.J., et al., 2021. Petrogenesis and geodynamic setting of the late Carboniferous granodiorite porphyry in Miaoergou pluton, southern West Junggar. Acta Petrol. Sin. 37 (4), 1159–1176. https://doi.org/10.18654/1000-0569/2021.04.12 (in Chinese).

Elliott, T., Plank, T., Zindler, A., et al., 1997. Element transport from slab to volcanic front at the Mariana arc. J. Geophys. Res. 102 (14), 991–1015. https://doi.org/10.1029/97JB00788.

Geng, H.Y., Sun, M., Yuan, C., et al., 2011. Geochemical and geochronological study of early Carboniferous volcanic rocks from the West Junggar: petrogenesis and tectonic implications. J. Asian Earth Sci. 42 (5), 854–866. https://doi.org/10.1016/j.jseaes.2011.01.006.

Guo, L.S., Liu, Y.L., Wang, Z.H., et al., 2010. The zircons U-Pb LA-ICP-MS chronology of volcanic rocks in Baogutu Area, Western Junggar. Acta Petrol. Sin. 26 (2), 471–477 (in Chinese).

Han, B.F., Ji, J.Q., Song, B., et al., 2006. Late Paleozoic vertical growth of continental crust around the Junggar Basin, Xinjiang (I): Timing of pott-collision plutonism. Acta Petrol. Sin. 22 (5), 1077–1086 (in Chinese).

Hawkesworth, C., Turner, S., Peate, D., et al., 1997. Elemental U and Th variations in island arcrocks: implications for U-series isotopes. Chem. Geol. 139 (1–4), 207–221. https://doi.org/10.1016/S0009-2541(97)00036-3.

He, X.Y., Liu, Y., Xu, X.L., et al., 2017. Controlling factors of Carboniferous volcanic reservoirs and favorable reservoir prediction in Xiquan area, Junggar Basin. Lithologic Reservoirs 29 (3), 42–51. https://doi.org/10.3969/j.issn.1673-8926.2017.03.006 (in Chinese).

Hofmann, A.W., 1988. Chemical differentiation of the Earth: the relationship between mantle, continental crust, and oceanic crust. Earth Planet Sci. Lett. 90 (3), 297–314. https://doi.org/10.1016/0012-821X(88)90132-X.

Hoskin, P.W.O., Black, L.P., 2010. Metamorphic zircon formation by solid-state recrystallization of protolith igneous zircon. J. Metamorph. Geol. 18 (4), 423–439. https://doi.org/10.1046/j.1525-1314.2000.00266.x.

Hou, L.H., Zou, C.N., Liu, L., et al., 2012. Geologic essential elements for hydrocarbon accumulation within Carboniferous volcanic weathered crusts in northern Xinjiang, China. Acta Pet. Sin. 33 (4), 533–540. https://doi.org/10.7623/syxb201204001 (in Chinese).

Hou, L.H., Luo, X., Wang, J.H., et al., 2013. Weathered volcanic crust and its petroleum geologic significance: a case study of the Carboniferous volcanic crust in northern Xinjiang. Petrol. Explor. Dev. 40 (3), 257–265+274. https://doi.org/10.11698/PED.2013.03.01.

Jiang, R.F., Cha, M., Chen, Z.H., et al., 2013. Hydrocarbon accumulation stages and evolution of Carboniferous volcanic rocks in Karamay oil field. Journal of Xi 'an Shiyou University (Natural Science Edition) 28 (6), 27–33. https://doi.org/10.3969/j.issn.1673-064X.2013.06.005 (in Chinese).

Jiang, Z.B., Huang, J.X., Li, Y.J., Li, S.Y., Wang, T., Wang, J., Peng, N.H., 2023. New evidence on the stratigraphy and chronology of 2140~3551.63 m Well 424 section in Karamay Oilfield and "Basin–Mountain" stratigraphic comparison. Northwestern Geology 56 (2), 1–9. https://doi.org/10.12401/j.nwg.2022044.

Jiao, X.Q., Zhang, G.L., Nin, H.P., et al., 2022. Genesis of Carboniferous volcanic rocks in northeastern Junggar Basin: new insights into the Junggar Ocean closure. Earth Sci. Front. 29 (4), 385–402. https://doi.org/10.13745/j.esf.sf.2021.12.2 (in Chinese).

Klein, E.M., Karsten, J., 1995. Ocean-ridge basalts with convergent-margin geochemical affinities from the Chile ridge. Nature 374 (6517), 52–57. https://doi.org/10.1038/374052a0.

Kröoner, A., Zhai, M.G., Zhang, L., 2020. Where and when did the Paleo-Asian ocean form? Precambr. Res. 349, 105840. https://doi.org/10.1016/j.precamres.2020.105840.

Kuang, L.C., Xue, X.K., Zou, C., et al., 2007. Oil accumulation and concentration regularity of volcanic lithostratigraphic oil reservoir: a case from upper-pLate Carboniferous of KA-BAI fracture zone Junggar Basin. Petrol. Explor. Dev. 34 (3), 285–290 (in Chinese).

Li, C., Ji, H.C., Jin, J., et al., 2017. Reservoir characteristics and distribution of upper Carboniferous inner volcanic rocks in Ke-Bai Fault Zone, Junggar Basin. J. Palaeogeogr. 19 (4), 677–691. https://doi.org/10.7605/gdlxb.2017.04.053 (in Chinese).

Li, J., 2008. Study on Reservoir Distribution and Control Factors of Carboniferous Volcanic Reservoirs in Northwest Margin of Junggar Basin. China University of Geosciences, Beijing. PhD dissertation 1–40 (in Chinese).

Li, J.Y., He, G.Q., Xu, X., et al., 2006. Crustal tectonic framework of Northern Xinjiang and adjacent regions and its formation. Acta Geol. Sin. 80 (1), 148–168 (in Chinese).

Li, Y.J., Xu, Q., Yang, G.H., et al., 2016. Intracontinental "lagged arc volcanic rocks" and its geological significance: evidence from early Permian lagged arc magmatism in northern Urho area of Western Junggar. Earth Sci. Front. 23 (4), 190–199. https://doi.org/10.13745/j.esf.2016.04.016 (in Chinese).

Li, Y.J., Wang, P.L., Zhi, Q., et al., 2024. Geochronology, geochemistry and geological significance of multi-porphyritic alkaline basalt from Hala'alate formation in Urho area, West Junggar, Xinjiang. Acta Petrol. Sin. 40 (7), 2037–2055. https://doi.org/10.18654/1000-0569/2024.07.03 (in Chinese).

Liu, W.F., Tang, C.Y., Zhang, X.Y., et al., 2019. Structural characteristics of the Triassic BaiJiantan formation in Bai21 well area. China Petroleum and Chemical Standards and Quality 24, 2 (in Chinese).

Liu, X.J., Xu, J.F., Wang, S.Q., et al., 2009. Geochemistry and dating of E-MORB type mafic rocks from Dalabute ophiolite in West Junggar, Xinjiang and geological implications. Acta Petrol. Sin. 25 (6), 1373–1389 (in Chinese).

Ludwig, K.R., 2003. User's manual for isoplot 3.0: a geochronological toolkit for Microsoft Excel. Berkeley Geochronology Center Special Publication.

Luo, X., Luo, M.G., Lin, J., et al., 2013. Reservoir characteristics of Carboniferous volcanic rocks in Liuqi area, Karamay Oilfield. J. Mineral. Petrol. 33 (2), 102–108. https://doi.org/10.19719/j.cnki.1001-6872.2013.02.014 (in Chinese).

Meschede, M., 1986. A method of discriminating between different types of mid-ocean ridge basalts and continental tholeiites with the Nb-Zr-Y diagram. Chem. Geol. 56, 207–218. https://doi.org/10.1016/0009-2541(86)90095-9.

Middlemost, E.A.K., 1972. A simple classification of volcanic rocks. Bull. Volcanol. 36 (2), 382–397. https://doi.org/10.1007/BF02596878.

Pan, H., Li, X.S., Qian, C.C., et al., 2022. Reservoir characteristics and reservoirforming rules of Carboniferous insider volcanic rocks in Kebai Fault Zone, Junggar Basin. J. Northeast Pet. Univ. 46 (1), 62–75. https://doi.org/10.3969/j.issn.2095-4107.2022.01.006 (in Chinese).

Pearce, J.A., 1982. Trace Elements Characteristic of Lavas from Destructive Plate Boundaries. Andesites//Thorpe R S. Orogenic Andesites and Related Rocks. John Wiley & Sons, Chichester, England, pp. 525–548.

Pearce, J.A., 2008. Geochemical fingerprinting of oceanic basalts with applications to ophiolite classification and the search for Archean oceanic crust. Lithos 100, 14–48. https://doi.org/10.1016/j.lithos.2007.06.016.

Pearce, J.A., Cann, J.R., 1973. Tectonic setting ot basic volcanic rocks determined using trace element analyses. Earth Planet Sci. Lett. 19, 290–300. https://doi.org/10.1016/0012-821X(73)90129-5.

Pearce, J.A., Lippard, S.J., Roberts, S., 1984. Characteristics and tectonic significance of supra-subduction zone ophiolites. Spec. Publ. Geol. Soc. Lond. 16 (1), 77–94. https://doi.org/10.1144/GSL.SP.1984.016.01.06.

Peccerillo, A., Taylor, S.R., 1976. Geochemistry of Eocene calc-alkaline volcanic rocks from the Kastamonu area, northern Turkey. Contrib. Mineral. Petrol. 58, 63–81. https://doi.org/10.1007/BF00384745.

Plank, T., Langmuir, C.H., 1988. An evaluation of the global variations in the major element chemistry of arc basalts. Earth Planet Sci. Lett. 90 (4), 349–370. https://doi.org/10.1016/0012-821X(88)90135-5.

Qiu, Z.K., Li, T., Yang, X., et al., 2020. Inside hydrocarbon accumulation characteristics of Carboniferous system in Ke-Bai fault zone, Junggar Basin. J. Southwest Pet Univ. (Natural Science Edition) 42 (5), 39–47 (in Chinese).

Safonova, I., Kotlyarov, A., Krivonogov, S., et al., 2017. Geochemistry of aluminous Atype granites along darabut tectonic belt in West Junggar, Xinjiang. Geochimica 35 (1), 55–67. https://doi.org/10.1007/s11442-006-0415-5.

Shao, L.F., Yu, F.S., Wang, D.D., et al., 2022. Geochronology, geochemistry, and tectonic significance of Carboniferous andesite in the zhongguai uplift, Northwestern Margin of the Junggar Basin. Geoscience 36 (3), 812–823. https://doi.org/10.19657/j.geoscience.1000-8527.2022.024.

Shen, P., Pan, H.D., Xiao, W.J., et al., 2013. Early Carboniferous intra-oceanic arc and back-arc basin system in the West Junggar, NW China. Int. Geol. Rev. 55 (16), 1991–2007. https://doi.org/10.1080/00206814.2013.810385.

Shervais, J.W., 1982. Ti-V plots and the petrogenesis of modern and ophiolitic lavas. Earth Planet Sci. Lett. 59, 101–118. https://doi.org/10.1016/0012-821X(82)90120-0.

Singer, B., Jicha, B., Leeman, W.P., et al., 2007. Along-strike trace element and isotopic variation in Aleutian Island arc basalt: subduction melts sediments and dehydrates serpentine. J. Geophys. Res. Solid Earth 112 (B6), B06206. https://doi.org/10.1029/2006JB004897.

Song, B., Zhang, Y.H., Wan, Y.S., et al., 2002. Mount making and procedure of the SHRIMP dating. Geol. Rev. 48 (S1), 26–30. https://doi.org/10.16509/j.georeview.2002.s1.007.

Su, Y.P., Tang, H.F., Hou, G.S., et al., 2006. Geochemistry of aluminous A-type granites along darabut tectonic belt in West Junggar, Xinjiang. Geochimica 35 (1), 55–67. https://doi.org/10.1007/s11442-006-0415-5.

Su, Y.P., Zheng, J.P., Griffin, W.L., et al., 2010. Zircon U-Pb and Hf isotopes of volcanic rocks from the Batamayineishan formation in the eastern Junggar basin. Chin. Sci. Bull. 55 (30), 2933–2945. https://doi.org/10.1007/s11434-010-4151-y (in Chinese).

Sun, S.S., McDonough, W.F., 1989. Chemical and isotopic systematics of oceanic basalts: Implications for mantle composition and process. In: Saunders, A.D., Norry, M.J. (Eds.), Magmatism in the Ocean Basins, 42. Special Publications of the Geological Society, London, pp. 313–345.

Tang, G.J., Wang, Q., Wyman, D.A., et al., 2010. Ridge subduction and crustal growth in the Central Asian Orogenic Belt: evidence from late Carboniferous adakites and high-Mg diorites in the Western Junggar region, northern Xinjiang (west China). Lithos 277 (3–4), 281–300. https://doi.org/10.1016/j.lithos.2010.01.004.

Tang, G.J., Wang, Q., Wyman, D.A., et al., 2012. Late Carboniferous high Nd(t)-Hf(t) granitoids, enclaves and dikes in Western Junggar, NW China: ridge-subduction-related magmatism and crustal growth. Lithos 140, 86–102. https://doi.org/10.1016/j.lithos.2012.01.025.

Tatsumi, Y., Kogiso, T., 2003. The subduction factory: its role in the evolution of the Earth's crust and mantle. Spec. Publ. Geol. Soc. Lond. 219 (1), 55–80. https://doi.org/10.1144/GSL.SP.2003.219.01.03.

Tong, L.L., 2023. The Chronology, Geochemical Characteristics and Petrogenesis of Volcanic Rocks of Hala'Alate Formation in Urho. Chang'an University, PhD dissertation. https://doi.org/10.26976/d.cnki.gchau.2023.000033 (in Chinese).

Wang, R., Zhu, Y.F., 2007. Geology of Baobei gold deposit in Western Junggar and the SHRIMP age of zircon rocks containing ore deposits. J. Geol. China Univ. 3, 590–602. https://doi.org/10.1007/s11430-007-0084-7 (in Chinese).

Wang, Y.W., Li, Y.J., Wang, P.L., et al., 2024. Volcanic rock assemblage, stratigraphic attribution and geo-logical significance of volcanic reservoir in Kebai Fault trough in Karamay: Constraints from well Gu 66. Northwest. Geol. 57 (5), 209–223. https://doi.org/10.12401/j.nwg.2023197 (in Chinese).

Wang, Z.P., Lv, Y., Li, H., Li, Y.J., Zhou, Y.L., Li, G.Y., Yang, G.X., 2021. Petrogenesis of Early Carboniferous alkaline basalt from the Wusun Mountain: Implications for tectonic evolution of the western Yining Block, NW China. Acta Geologica Sinica 95 (4), 1125–1138. https://doi.org/10.1111/1755-6724.14382.

Wei, S.N., Zhu, Y.F., An, F., 2014. Mineralization and elements migration characteristics of porphyry copper deposits in Baogutu area, Xinjiang. Miner. Depos. 33 (1), 165–180. https://doi.org/10.3969/j.issn.0258-7106.2014.01.010 (in Chinese).

Williams, I.S., 1998. U-Th-Pb geochronology by ion microprobe. In: McKibben, M.A., Shanks, I.I.I.W.C., Ridley, W.I. (Eds.), Applications of Microanalytical Techniques to Understanding Mineralizing Processes, 7. Reviews in Economic Geology, pp. 1–35. https://doi.org/10.2113/gsecongeo.96.8.1587.

Winchester, J.A., Floyd, P.A., 1977. Geochemical discrimination of different magma series and their differentiation products using immobile elements. Chem. Geol. 20 (4), 325–343. https://doi.org/10.1016/0009-2541(77)90057-2.

Wood, D.A., 1980. The application of a Th-Hf-Nb diagram to problems of tectomagmatic classification and to establishing the nature of crustal contamination of the British Tertiary volcanic provinic. Earth Planet Sci. Lett. 50, 11–30. https://doi.org/10.1016/0012-821X(80)90116-8.

Wright, J.B., 1969. A simple alkalinity ratio and its application to questions of nonorogenic granite genesis. Geol. Mag. 106 (4), 370–384.

Wu, H.W., Su, Z.T., Pei, W.C., et al., 2024. Zircon SHRIMP U-Pb ages and Hf isotope characteristics of the zircons from tuff in Ordovician Majiagou formation in thecentral—Eastern Ordos basin and their geological significance. Geol. Rev. 70 (5), 1767–1787. https://doi.org/10.16509/j.georeview.2024.05.008 (in Chinese).

Xia, L.Q., Li, X.M., 2019. Basalt geochemistry as a diagnostic indicator of tectonic setting. Gondwana Res. 65, 43–67. https://doi.org/10.1016/j.gr.2018.08.006.

Xiang, K.P., Li, Y.J., Xu, L., et al., 2013. The definition of Chengjisihanshan formation and its significances in Baijiantan region, West Junggar, Xinjiang. Northwest. Geol. 46 (2), 63–68 (in Chinese).

Xiang, K.P., Li, Y.J., Li, Z., et al., 2015. LA-ICP-MS zircon age and geochemistry of the Aladeyikesai formation volcanic rocks in the Halaalate Mountain of West Junggar, Xinjiang, and their tectonic significance. Acta Geol. Sin. 89 (5), 843–855 (in Chinese).

Xiao, Y., Liu, X.J., Zhang, Z.G., et al., 2023. Junggar intra-oceanic arc magmatism: constrains from geochemistry and sr-nd-hf isotope geochemistry of the early Carboniferous Baikouquan volcanic rocks in West Junggar, NW China. Geotect. Metallogenia 47 (1), 214–232. https://doi.org/10.16539/j.ddgzyckx.2022.01.011.

Xinjiang Oilfield, 2022. Research Report on the Carboniferous Formation and Evolution in the Kelamayi-Wuerhe Region and its Response and Correlation Within the Basin (in Chinese).

Xinjiang Oilfield, 2025. Research Report on the Carboniferous Sequence and Reservoir Characteristics of the Upper Plate of the Kebei Fault (in Chinese).

Xu, X.Y., Li, R.S., Chen, J.L., et al., 2014. Some understandings of Paleozoic tectonic evolution in northern Xinjiang. Acta Petrol. Sin. 30 (6), 1521–1534. https://doi.org/10.1007/s11430-007-0084-7 (in Chinese).

Yang, G.X., Li, Y.J., Tong, L.L., et al., 2016. Petrogenesis and tectonic implications of early Carboniferous alkaline volcanic rocks in Karamay region of West Junggar, Northwest China. Int. Geol. Rev. 58 (10), 1278–1293. https://doi.org/10.1080/00206814.2016.1149781.

Yi, Z.J., He, D.F., 2018. Tectono-stratigraphic sequence and basin evolution of the eastern Junggar Basin. Oil Gas Geol 39 (5), 932–942. https://doi.org/10.11743/ogg20180508.

Yin, J.Y., Chen, W., Yuan, C., et al., 2015. Petrogenesis of Early Carboniferous adakitic dikes, Sawur region, northern West Junggar, NW China: implications for geodynamic evolution. Gondwana Res 27 (4), 1630–1645. https://doi.org/10.1016/j.gr.2014.01.016.

Yin, J.Y., Yuan, C., Sun, M., et al., 2012. Age, geochemical features and possible petrogenesis mechanism of Early Permian magnesian diorite in Hatu, Xinjiang. Acta Petrol. Sin. 28 (7), 2171–2182 (in Chinese).

Yu, C.M., Zheng, J.P., Tang, Y., et al., 2004. Reservoir properties and effect factors on volcanic rocks of basement beneath Wucaiwan depression, Junggar Basin. Earth Sci 29 (3), 303–308. https://doi.org/10.3321/j.issn:1000-2383.2004.03.007 (in Chinese).

Zartman, R.E., Doe, B.R., 1981. Plumbotectonics-The model. Tectonophysics 75 (1), 135–162. https://doi.org/10.1016/0040-1951(81)90213-4.

Zhang, J.E., Xiao, W.J., Han, C.M., et al., 2011. A Devonian to Carboniferous intra-oceanic subduction system in Western Junggar, NW China. Lithos 125 (1–2), 592–606. https://doi.org/10.1016/j.lithos.2011.03.013.

Zhang, J.E., Xiao, W.J., Luo, J., et al., 2018. Collision of the Tacheng block with the Mayile-Barleik-Tangbale accretionary complex in Western Junggar, NW China: Implication for early-middle Paleozoic architecture of the Western Altaids. J. Asian Earth Sci. 159, 259–278. https://doi.org/10.1016/j.jseaes.2018.04.005.

Zhang, L., 2020. Geological Structure, Filling and Genetic Mechanism of Carboniferous Basin in Junggar Area. China University of Geosciences, Beijing. PhD dissertation (in Chinese).

Zhang, L.C., Wan, B., Jiao, X.J., et al., 2006. Characteristics and geological significance of adakitic rocks in copper-bearing porphyry in Baogutu, Western Junggar. Geol. China 33 (3), 626–631. https://doi.org/10.12029/gc20060320 (in Chinese).

Zhang, Y.Q., Chen, Z.H., Tang, Y., et al., 2014. Characteristics of volcanic reservoirs in the Junggar Basin-Bai Fault Zone. Acta Sedimentol. Sin. 32 (4), 754–765. https://doi.org/10.14027/j.cnki.cjxb.2014.04.015.

Zheng, J.P., Min, S., Zhao, G.C., et al., 2007. Elemental and Sr-Nd-Pb isotopic geochemistry of late Paleozoic volcanic rocks beneath the Junggar basin, NW China: implications for the formation and evolution of the basin basement. J. Asian Earth Sci. 29 (5–6), 778–794. https://doi.org/10.1016/j.jseaes.2006.05.004.

Zhou, G.F., Zhao, J.Z., Ding, C.H., et al., 2023. Structural evolution and hydrocarbon enrichment characteristics of Kebai Fault Zone, Junggar Basin. In: Proceedings of the International Petroleum and Petrochemical Technology Conference, 7. https://doi.org/10.26914/c.cnkihy.2023.027641 (in Chinese).

Zhou, Y., Liang, T., Zhao, X.Y., et al., 2024. Identification markers and eruption patterns of volcanic rocks in different eruption environments: a case study of the Carboniferous system in eastern Junggar basin. J. Palaeogeogr. 26 (6), 1–23. https://doi.org/10.7605/gdlxb.2024.06.079.

Zhu, Y.F., Wang, T., Xu, X., 2007. Progress of geology study in Xinjiang and its adjacent regions. Acta Petrol. Sin. 23 (8), 1785–1794. https://doi.org/10.3969/j.issn.1000-0569.2007.08.001 (in Chinese).

Zindler, A., Hart, S., 1986. Chemical geodynamics. Annu. Rev. Earth Planet Sci. 14, 493–571. https://doi.org/10.1146/annurev.ea.14.050186.002425.